Ocean Modelling 74 (2014) 36–52

Contents lists available at ScienceDirect

Ocean Modelling

journal homepage: www.elsevier.com/locate/ocemod

The upper Bay of Bengal salinity structure in a high-resolution model

Rachid Benshila [a,*], Fabien Durand [b], Sébastien Masson [a], Romain Bourdallé-Badie [c], Clement de Boyer Montégut [d], Fabrice Papa [b,e], Gurvan Madec [a]

[a] LOCEAN/IPSL, UPMC/CNRS/IRD/MNHN, Paris, France
[b] LEGOS, IRD/CNRS/CNES/UPS, Toulouse, France
[c] MERCATOR Ocean, Parc Technologique du Canal, Ramonville Saint Agne, France
[d] IFREMER, LOS, F-29280 Brest, France
[e] Indo-French Cell for Water Sciences, IFCWS, IRD-IISc Joint International Laboratory, Indian Institute of Science, Bangalore, India

ARTICLE INFO

Article history:
Received 17 December 2012
Received in revised form 19 September 2013
Accepted 2 December 2013
Available online 10 December 2013

Keywords:
Salinity
Bay of Bengal
Export of fresh water plume
High resolution ocean modeling

ABSTRACT

Salinity in the Bay of Bengal is highly heterogeneous, with extremely fresh waters found at the surface in the Northern part of the basin, and saltier waters at subsurface as well as to the south. This paper investigates the seasonal structure of sea surface salinity of the Bay in a regional high-resolution model forced by ERA-Interim reanalysis and various precipitation products. Surface circulation is believed to drive the spreading of northern Bay of Bengal fresh waters to the rest of the Indian Ocean. We first present a series of experiments to infer the sensitivity of modeled circulation to various numerical choices. Surface circulation is found to be sensitive to the horizontal resolution of the model, with the 1/12° version appearing much more realistic than the 1/4° version. The sidewall boundary condition is also drastically influencing the characteristics of the western boundary current simulated. We then investigate the sensitivity of the salinity response to the various precipitation products. We observe that ERA-Interim excess precipitation induces a fresh bias in the surface salinity response. Spaceborne precipitation products are more satisfactory. We then identify the pathways of the northern Bay freshwater mass, based on passive tracers experiments. Our model suggests that over timescales of a few months, vertical exchanges between the upper fresh layer and the underlying saltier layer appear to be the main export pathway for the freshwater. The horizontal circulation within the mixed layer also acts to convey fresh waters out of the Bay at these timescales, but in a lesser quantity compared to the vertical export. Beyond its intrinsic interest for the understanding of Bay of Bengal physics, this study highlights the need for a careful design of any realistic numerical model, in three key aspects: the choice of the resolution of the model, the choice of the sub-grid scale parameterizations, and the choice of the forcing fluxes.

© 2013 Elsevier Ltd. All rights reserved.

1. Introduction

Salinity of the Bay of Bengal (hereafter termed as the Bay) is highly heterogeneous, both on the horizontal and on the vertical. Downward increase of 5 units (in the PSS-78 scale) over the upper 20 m of the water column is not uncommon in the open Bay (e.g. Vinayachandran and Kurian, 2007). On the horizontal, it is characterized by extremely fresh waters in the North and North-Eastern parts, in response to excess freshwater supply from both continental rivers and from oceanic precipitation, and saltier waters in the South-central Bay. The fresh waters spread as a thin cap (typically: 10 to 20 m thick), and invade the northern half of the bay (Vinayachandran and Kurian, 2007). Horizontal gradients as high as 1 unit every 20 km were observed at the southern edge of this freshwater plume (e.g. Shetye, 1993). The fresh cap has profound implications on the air-sea exchanges, and thus on the climate of the neighbouring continents. First, the enhanced vertical stability of the upper surface layer is conducive to a trapping of the atmospheric heat at the ocean surface, and maintains high sea surface temperatures (SSTs) throughout the year (Han and McCreary, 2001; Shenoi et al., 2002). These high SSTs, in turn, are believed to favour atmospheric convective activity and freshwater supply, hereby creating a positive feedback. In particular, it has been suggested that the salinity stratification prevents the oceanic cooling effect during the development of atmospheric cyclones, hence favouring intense cyclones (Sengupta et al., 2008; Neetu et al., 2012). Second, salinity also has the potential to influence the amplitude of intra-seasonal variability of the SST in the Northern Bay (Vinayachandran et al., 2012).

In average, the Bay receives about twice as much freshwater (around 80% from oceanic precipitation and 20% from continental runoff) as it evaporates back to the atmosphere (de Boyer

* Corresponding author. Address: LOCEAN, IPSL, Univ. Pierre et Marie Curie, Case 100, Couloir 45-55, 4ème, Piece 429, 4, Place Jussieu, 75252 Paris, France. Tel.: +33 1 (01) 44277161; fax: +33 1 (01) 44273805.
E-mail address: rachid.benshila@locean-ipsl.upmc.fr (R. Benshila).

1463-5003/$ - see front matter © 2013 Elsevier Ltd. All rights reserved.
http://dx.doi.org/10.1016/j.ocemod.2013.12.001

Montégut, 2005, its Fig. 48). Given that the basin is closed by the Asian landmass at its northern boundary (Fig. 1), it has to export its excess freshwater southward via the oceanic circulation. The exact processes and pathways responsible for this export are poorly documented, on account of a lack of adequate observational information. On one hand, most of what has been published in the observational field so far relies either on point-wise oceanic time series (e.g. Murty et al., 1996; Vinayachandran et al., 2002; Webster et al., 2002) or on occasional synoptic transects (Shetye et al., 1991, 1996; Shetye, 1993; Vinayachandran and Kurian, 2007; Parampil et al., 2010). Beyond the large-scale North–South gradient, all these studies point out that sea surface salinity (SSS) is structured at small scale throughout the basin, with sharp fronts in all seasons. They conclude that the eddy and filaments-induced advection dominate over the atmospheric freshwater fluxes to drive the local rate of change of SSS. On the other hand, modelling the salinity structure of the Bay has been fairly challenging, for three main reasons. First, this demands an accurate knowledge of the freshwater exchanged with the atmosphere and received from the surrounding continents. While the former is known with acceptable accuracy from spaceborne datasets and/or atmospheric reanalyses (e.g. Yu and McCreary, 2004), the latter has been very poorly observed (Shankar, 2000; Durand et al., 2007). With more than 60% of the total continental freshwater received by the Bay (Sengupta et al., 2006), the Ganges and Brahmaputra rivers are the main contributors. Very recently, some in situ discharge datasets of these two rivers have been released (Jian et al., 2009). This, combined with high resolution satellite altimetry over the rivers, allowed to produce consistent, accurate and interannual time series of total discharge at their mouth, directly usable for ocean modelling (Papa et al., 2010, 2012). The second hurdle for ocean modelers concerned the availability of salinity observations to validate the numerical solutions. As far as in situ observations are concerned, the tropical Indian Ocean is, by far, the least surveyed of the three tropical basins. In addition, the national Exclusive Economic Zones occupy a large fraction of the domain, and some data policy issues prevent the community from accessing all the existing databases. We can nevertheless rely on the advent of Argo programme, the fleet of autonomous profilers sampling the Bay increasing gradually from 2004 onwards. Nowadays the spatial coverage is close to nominal, with one float every 300 km on average. As shall be seen in this paper, this fleet – in addition to the historical hydrographic databases – samples adequately the large-scale seasonal patterns of salinity in the Bay. It is thus of prime relevance for model validation. One more step in the development of the Bay observing system has been completed recently, with the recent launch of SMOS (November 2009) and AQUARIUS (June 2011) satellites dedicated to spaceborne monitoring of SSS. The third limitation of ocean models of the Bay concerns their resolution. Mesoscale eddies are ubiquitous in the Bay (e.g. Durand et al., 2008, 2009). Given that they have a clear signature in the patterns of SSS variability, they need to be resolved by the models. This, in particular, precludes the use of models with grid resolutions of order 0.5°, which essentially simulate a laminar flow (Durand et al., 2011). This puts a stringent constraint on the size of the numerical problem, and on the computing resources needed to solve it. Over the past few years, however, eddy-resolving models (with grid size of order 10 km) gradually became sufficiently mature to make the realistic modelling of the ocean tractable. The circulation of the Bay, in particular, was studied by Diansky et al. (2006) and Wu et al. (2007), using eddy-resolving models implemented on the Indian sector only and on the global ocean, respectively. None of these two studies, however, investigated the specific benefit of the high resolution over coarser models in order to simulate the circulation of the Bay. They did not attempt to analyze the realism of their SSS solution either, as both models used a strong relaxation towards observed climatological fields.

The Bay of Bengal appears as a relevant and challenging testcase to investigate the sensitivity of an ocean general circulation model to the various possible numerical choices available to the user. To illustrate the importance of a proper resolution of the model, we first investigate the basic features of the circulation of the Bay by comparing various versions of an eddy-resolving (1/12°) ocean model, along with a coarser one (1/4°). We then investigate specifically the issue of realistic modelling of SSS, by carrying out a series of sensitivity experiments in the eddy-resolving model. This is, to our knowledge, a first attempt to do so, over this part of the world ocean. Section 2 presents the numerical framework. Section 3 discusses the dynamics of the eddy-resolving model and its coarser counterpart. In Section 4, we analyze the sensitivity of the model SSS to the precipitation flux. Section 5 investigates the fate of the freshwater plume. Section 6 synthesizes our findings.

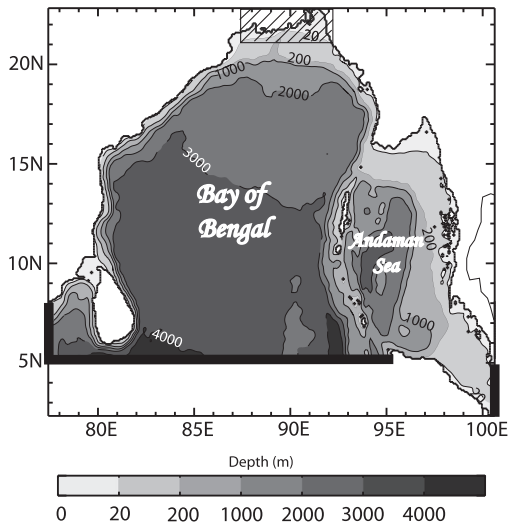

Fig. 1. Model domain and bathymetry. The three black thick lines feature the location of the open boundaries of the model. The hatched rectangle in the northern Bay delineates the location of the mouths of Ganges–Brahmaputra river system.

2. The model

The model used here is NEMO (Nucleus for European Modelling of the Ocean) described by Madec (2008). It solves the set of primitive equations where the tracers (temperature and salinity) and the horizontal component of the velocities are prognostic variables and the vertical velocity is diagnosed through the continuity equation. The equations are discretized on an Arakawa C-grid. There is a free surface, with no explicit splitting between baroclinic and barotropic velocities but an additional force is computed to damp external gravity waves (Roullet and Madec, 2000). Such a force is in phase quadrature with the surface pressure gradient and acts like a low order time filter for phenomena with a time scale lower than the baroclinic time step. This formulation has the advantage of conserving the oceanic salt content, unlike rigid-lid ocean models. Temporal integration is performed by a leap-frog scheme with Asselin filtering.

The base configuration we mainly use in this study (henceforth termed as BB12) covers the entire Bay of Bengal from 2.25°N to 22.8°N, 77.3°E to 100°E (Fig. 1). We use a Mercator grid, quasi-isotropic as these latitudes, with a resolution of 1/12°. In the vertical, we resolve 50 z levels with partial steps, Δz varying from 1 m to 450 m, with higher resolution at the top (we have 8 levels in the upper 10 m). The upper 100 m of the vertical grid are displayed

on Table 1. The bottom topography has been built with ETOPO-2 mixed with GEBCO near the shelf areas.

The open boundaries are handled using a radiation-relaxation approach (following Marchesiello et al., 2001), where we use the radiation condition to determine whether a boundary is passive (outward propagation) or active (inward propagation). Thus, if we consider a prognostic variable ϕ and its phase velocity $(C_{\phi x}, C_{\phi y})$ in the normal and tangential direction:

$$C_{\phi x} = \frac{-\phi_t}{(\phi_x^2 + \phi_y^2)}\phi_x \quad C_{\phi y} = \frac{-\phi_t}{(\phi_x^2 + \phi_y^2)}\phi_y$$

We retain only the normal component of the velocity (but ϕ_y in the computation of $C_{\phi x}$). The boundary conditions are then updated differently depending the sign of ϕ_x.

If passive, the radiation condition is applied. In active case, the solution is nudged toward external data. Finally, for instance our southern OBC is updated as follows:

$$\phi_t = -C_{\phi x}\phi_x + \frac{1}{\tau_o}(\phi_c - \phi) \quad (C_{\phi x} < 0)$$
$$\phi_t = \frac{1}{\tau_i}(\phi_c - \phi) \quad (C_{\phi x} > 0)$$

where τ_i corresponds to a strong relaxation (1 day) toward input data and τ_o to a weak relaxation (order of 1000 days), to avoid shocks when changing from active to passive mode. The radiation condition is applied to the model variables: temperature, salinity, tangential and normal velocities. For normal and tangential velocities, u and v, radiation is applied with phase velocities calculated from u and v respectively. For the radiation of tracers, we use the phase velocity calculated from the tangential velocity in order to avoid calculating too many independent radiation velocities and because tangential velocities and tracers have the same position along the boundary on a C-grid.

Input boundary data are three day frequency from a global 1/12° interannual simulation performed at Mercator-Ocean, hereafter termed as ORCA12. ORCA12 and BB12 grids strictly coincide throughout the Bay of Bengal domain of BB12. As shall be seen in Section 3, the radiative open boundaries allow the coastal Kelvin waves emanating from the equatorial waveguide to freely enter our domain at its south-eastern edge; they also allow the advection of heat and salt out of the domain. The northern boundary is closed by the Asian landmass. An eastern open boundary was introduced in the Malacca strait (at 101°E) for the sake of consistency with the global ORCA12 simulation but it bears a negligible throughflow (not shown). Advection of temperature and salinity is performed with a total variation diminishing scheme (Lévy et al., 2001) and we chose a vector invariant formulation for momentum, conserving total enstrophy and kinetic energy (Penduff et al., 2007; Le Sommer et al., 2009). Horizontal subgrid-grid scale physics is parameterized via an isoneutral laplacian operator on tracers ($100\ m^2\ s^{-1}$) and a bilaplacian operator for momentum ($10^{10}\ m^4\ s^{-1}$). The lateral boundary condition for momentum is discussed in part 3.

Vertical eddy coefficients are computed from an embedded 1.5 turbulent closure model where one resolves a prognostic equation for the turbulent kinetic energy with a closure assumption (Blanke and Delecluse, 1993) with a background value of $10^{-5}\ m^2\ s^{-1}$. The time evolution of the turbulent kinetic energy E is the result of the production of E through vertical shear, its destruction through stratification, its vertical diffusion, and its dissipation of Kolmogorov type:

$$\frac{dE}{dt} = K_z\left(\left(\frac{\partial u}{\partial z}\right)^2 + \left(\frac{\partial v}{\partial z}\right)^2 + \frac{g}{\rho_0}\frac{\partial \rho}{\partial z}\right) + \Delta_{3D}(E) - \frac{c_\varepsilon E^{3/2}}{l_\varepsilon}$$

$$K_z = c_k l_k E^{1/2}$$

where K_z is the vertical eddy diffusivity coefficient, l_ε the dissipation scale, l_k the mixing scale, c_ε and c_k constants (respectively 0.7 and 0.1).

The mixing and dissipation scale l_k and l_ε are first evaluating following:

$$l_k = l_\varepsilon = \sqrt{2E}/N \text{ with } N \text{ the Brunt-Vaisälä frequency}$$

then bounded such as their vertical variations cannot be larger than the variation of depth.

At sea surface, no SSS restoring is applied on salinity, which allows us to properly diagnose the salinity response to freshwater forcing. Surface fluxes are computed using CORE bulk formulae (Large and Yeager, 2004). To force the model, we first use 6-hourly ERA-Interim (Dee et al., 2011) interannual reanalysis for momentum, heat and freshwater fluxes to assess the sensitivity of the model to our numerical choices (Section 3). It is known that a careful choice of the momentum fluxes is a must for a proper simulation of the Northern Indian Ocean circulation (Kantha et al., 2008). The choice of ERAinterim momentum forcing comes from the various sensitivity experiments carried out with our model at global scale in the Drakkar project (Drakkar group, 2007). We then consider various precipitation products in conjunction with ERA-Interim precipitation flux (Section 4). River runoffs are taken from Bourdalle-Badie and Tréguier (2006), with the exception of Ganges and Brahmaputra discharges that vary interannually (Papa et al., 2010; Durand et al., 2011). Irrawaddy river (reaching the Bay in the Northern Andaman Sea) does not vary interannually, despite its magnitude comparable to the Ganges river, because no reliable interannual data exist for its discharge. All rivers are injected in the ocean model as surface precipitation at river mouth with enhanced vertical mixing to parameterize unresolved scales, using a vertical mixing coefficient of $10^{-3}\ m^2\ s^{-1}$ over the first 12 m.

In order to investigate the sensitivity of the modeled circulation to the horizontal resolution (Section 3), we follow a twin-experiment approach, using a global simulation at 1/4° (hereafter ORCA025) performed at Mercator-Ocean with similar numerical settings and forcing choices, except for diffusion and viscosity coefficient, for obvious stability reasons. The setting of the various sensitivity experiments is summed up in Table 2.

Due to its geographic location and its limited size (less than 2000 km of zonal extent, see Fig. 1), our ocean model rapidly adjusts to the forcing. This allows carrying out quite short spinups (typically: a few months long), as compared to other tropical basins. Thus, we integrated the model over the 1/2002–12/2006 per-

Table 1
Vertical discretization of the upper 100 m of the water column in our model.

Level	1	2	3	4	5	6	7	8	9	10	11
Depth (m)	0.5	1.5	2.6	3.8	5.0	6.4	7.9	9.6	11.4	13.5	15.8
Level	12	13	14	15	16	17	18	19	20	21	22
Depth (m)	18.5	21.6	25.2	29.4	34.4	40.3	47.4	55.8	65.8	77.8	92.3

Table 2
Configurations name and settings used for sensitivity tests and experiments. Full gray correspond to experiments not performed, red to the final one leading to conclusion in Section 6.

Name	ORCA025	BB12	BB12_ns	BB12_ps	Section
Resolution	1/4°	1/12°	1/12°	1/12°	3
Side wall	Free slip	Free slip	No slip	Partial slip	3
Viscosity	10^{11} m^4 s^{-1}	10^{10} m^4 s^{-1}	10^{10} m^4 s^{-1}	10^{10} m^4 s^{-1}	3
Forcing for dynamics sensisivity	ERAI	ERAI	ERAI	ERAI	3
Forcing for salinity response		ERAI			4
		GPCP			
		DFS4			
		TMI			
Forcing for freshwater study		TMI			5

iod, starting from rest (and from Levitus climatology for tracers) in January 2002. In this study, we analyse the 1/2003–12/2006 period. The annual cycle being dominant in the upper ocean variability (in response to the monsoonal forcing), over most of the study we consider the seasonal climatology computed from this 4 year long period. All simulations were performed on three NEC SX8 processors, with an execution time of 5 h per year of simulation. Tests performed on IBM Power6 processors have shown an equivalent elapsed time on 16 processors, with still good scalability on a higher number of cores.

3. Dynamical response to numerical choices

Performing sensitivity tests of a general circulation model over a given area is often a tedious task, and particularly so at high resolution where computing resources are an issue. However, we will show in this section that it is a compulsory step, which drastically conditions the realism of the numerical outputs of the model. We specifically investigate the sensitivity of the circulation of our model to two key-characteristics of its numerics: the horizontal resolution (Section 3.1) and the sidewall dynamical boundary condition (Section 3.2). Table 2 summarizes the set of numerical experiments we carried out.

3.1. Impact of the horizontal resolution

Fig. 2 compares the seasonal cycle of surface circulation of the Bay for the two resolutions, along with the GECKO observed product of Sudre et al. (2013). This product is a combination of the geostrophic flow (deduced from altimetry) and Ekman flow (deduced from Quickscat winds). It has been fully validated against in situ eulerian and lagrangian current observations (see Sudre et al. (2013) for details). At basin-scale, the dominant signal is the seasonal reversal of the monsoon currents. At the western boundary lies the East India Costal Current (EICC). Between 10°N and 20°N, it flows poleward prior to summer monsoon, reverses during summer, and flows equatorward in fall. This is an intriguing timing, preceding that of the local wind by several months. Indeed, as will be discussed in the next paragraph, this current is partly remotely forced by the seasonal cycle of the winds in the Northern and interior Bay of Bengal and in the equatorial ocean (see e.g. Shankar et al. (2002) or Durand et al. (2009), for a synthesis of the existing literature on this issue). Over the interior Bay, the circulation is less contrasted. In April, it is roughly organized in a basin-scale counter-clockwise gyre, closing the northward boundary limb. In July, two eastward branches emerge from the western boundary, centered around 8°N and around 16°N. In November, the interior circulation is basically north-westward, and turns southward upon reaching the western boundary.

Both ORCA025 and BB12 reproduce adequately the observed features. The good consistency between the two models is not surprising, given that this variability is known to be largely wind-driven at large scale through linear physics (McCreary et al., 1993; Shankar et al., 2002). For both models, the seasonal cycle of the EICC is realistic throughout its domain, with in particular a reversal of the current (from poleward to equatorward) during fall and another (from equatorward to poleward) during winter. Basically, the seasonal dynamics of EICC consists of four different linear mechanisms: local alongshore winds, Ekman pumping in the interior Bay that generates westward-propagating Rossby waves, remote wind forcing along the Northern and Eastern boundary of the Bay, and remote wind forcing in the equatorial basin (McCreary et al., 1996; Shankar et al., 1996). The latter two mechanisms involve coastally-trapped Kelvin waves that propagate around the periphery of the Bay. It was shown that all of these forcings have some importance at one moment or another, during the seasonal cycle. The remote influence of equatorial wind, in particular, appears instrumental in the timing of the reversals of EICC. BB12, unlike ORCA025, has a domain that does not comprise the equatorial basin (Fig. 1); rather, the equatorial forcing enters BB12 via the southern open boundary condition. The seasonal cycle of EICC reversals in BB12 does not appreciably differ from that of ORCA025. It is also very similar to the variability simulated by the global counterpart of BB12 (ORCA12; not shown). This, in particular, validates the open boundary behaviour.

This result was expected, as the physics driving the variability of the monsoon current systems is known to have a much larger scale than the resolution of any of our two models (e.g. Shankar et al., 2002). However, the issue remain about the capability of the two models to simulate the shorter space scales of the oceanic flow (typically: the mesoscale turbulence). This mesoscale is indeed known to be ubiquitous in the Bay (Shenoi et al., 1999). To do so, Fig. 3 presents the variability of sea level observed by altimetry (the altimeter products were produced by Ssalto/Duacs and distributed by Aviso, with support from Cnes; http://www.aviso.oceanobs.com/duacs/), and simulated by the two models. The most remarkable difference between the two simulations lies in the amplitude of the simulated patterns: while ORCA025 underestimates the observed maxima by about 40%, BB12 manages to produce the proper level of variability, throughout the basin. The observations exhibit two regions of extremely high variability (values in excess of 0.18 m), one off the mouths of Ganges–Brahmaputra in the Head Bay, and one in the eastern Bay off the mouths of Irrawaddy at 15°N, 96°E. They might result from the halosteric effect of the seasonal input of freshwater from the two river systems. At basin scale, there is a contrasted pattern with high variability (in excess of 0.12 m) in a crescent-like region spanning the western Bay, roughly parallel to the coast, and a region of low variability (inferior to 0.06 m) in the South-central Bay. The region of high variability in the West is located to the east of the shelf break, in the deep ocean; it is separated from the coast by a narrow band of relatively low variability (around 0.1 m). The localized maximum in the eastern Bay, which appears as a very small scale pat-

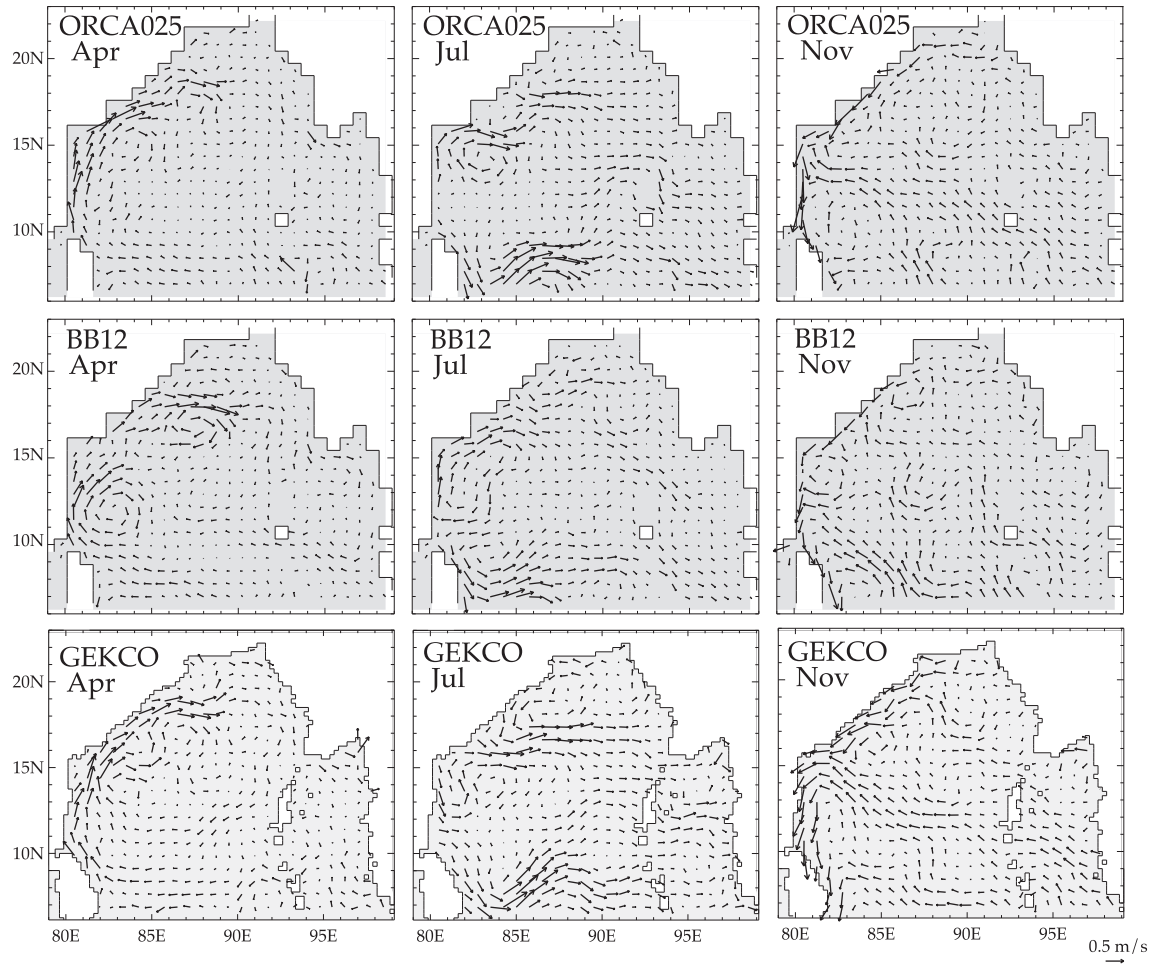

Fig. 2. (Top) Monthly climatology of the surface current simulated by ORCA025 model, for the pre-monsoon (April), monsoon (July) and post-monsoon season. The corresponding months are indicated. (middle) Same, for BB12 model. (bottom) Same, for the GEKCO observed product. All climatologies are computed over 2003–2006.

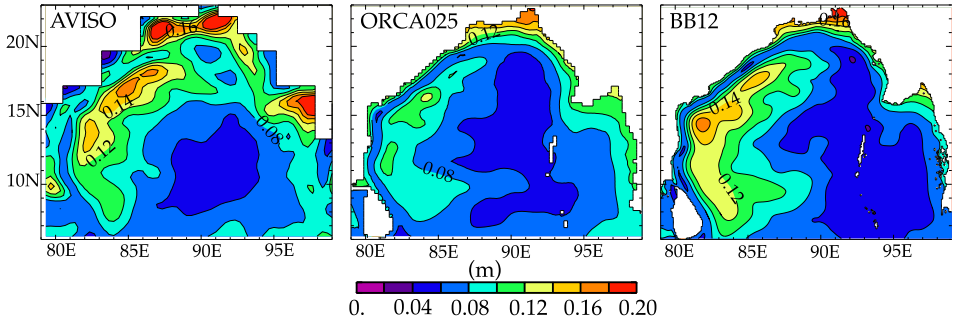

Fig. 3. Standard deviation (of SLA computed over 2003–2006 for (left) AVISO product, (centre) ORCA025 configuration and (right) BB12 configuration. Isocontours are every 0.02 m.

tern restricted to the northernmost extremity of the Andaman Sea, is not properly captured by the simulations. The reason for this is unclear. However, care must be taken when considering the observed maximum there, as gridded altimetry products are known to present serious drawbacks in the very shallow coastal regions of the Bay (Durand et al., 2008). In the absence of independent sea level observations there (such as tide-gauges measurements), it is hazardous to understand the discrepancy between both models and observations. In the western Bay, both models simulate the observed narrow band of low variability, located immediately to the West of the crescent of high variability. This band clearly delineates the location of the shelf break, from the Southern tip of Sri Lanka to about 20°N.

Another way to illustrate the difference between the two simulations can be done by computing the power spectra of their surface current, as compared with that of AVISO daily products (Fig. 4). The differences can be quantified first by the examination of the slope of the energy spectra, computed using a transform

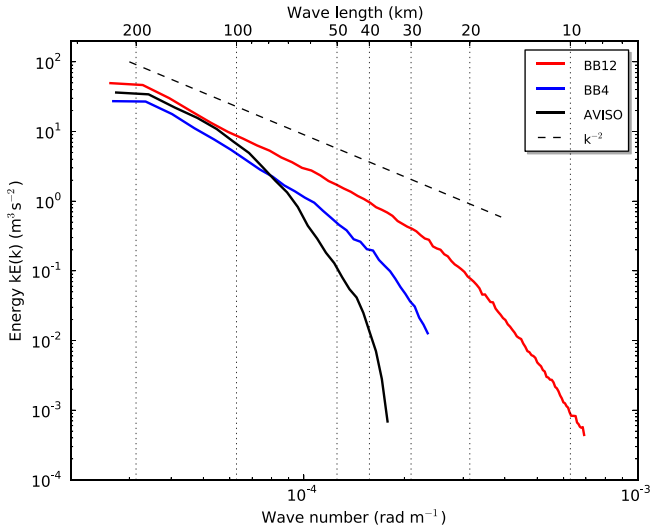

Fig. 4. Wavenumber spectrum of the modeled and observed surface current, computed over the region [7.5°N–17°N] [83°E–91°E] (see the text for details). Superimposed is the theoretical k^{-2} slope.

(Denis et al., 2002) suitable for limited area. Following Skamarock (2004) and Marchesiello et al. (2011), we identify the effective resolution of both models, as the transition between a quasi linear evolution in k^{-2} and a steep decay. This break indicates the wavelength under which the biharmonic diffusion operator begins to act and selectively dissipates the smallest scales. Both configurations show an effective resolution of about 8 times the grid scale, 200 km for ORCA025 (1/4° grid) and 60 km for BB12 (1/12° grid). In terms of amplitude ORCA025 shows less energy than BB12 at all scales. Indeed the effective resolution of BB12 allows to explicitly resolve the first baroclinic Rossby radius of 60 km (Chelton et al., 1998) in the area of the spectrum computation and confirm that our model is actually eddy resolving. Fig. 4 shows that the gridded observed sea-level product AVISO has less energy than our models at short space scales (shorter than 60 km).

From the above diagnostics, it appears that the highest horizontal resolution of BB12 allows to better represent the observed patterns of dynamical variability, particularly in the vicinity of the western and northern boundaries. The benefit is particularly evident at spatial scales ranging between 200 km and 60 km. In contrast, the fact that both models successfully reproduce the observed seasonal variability of the monsoon currents confirms that these currents are forced at large scale (Shankar et al., 2002).

3.2. Impact of the lateral momentum boundary condition

We now investigate the issue of the choice of the lateral momentum boundary condition at the coast. For ORCA025, the sidewall condition is free-slip, as it yields the most realistic boundary currents at the surface (Penduff et al., 2007; Le Sommer et al., 2009). The free-slip condition assumes that the tangential velocity at the coast is equal to the offshore velocity. This numerical choice may be seen as a convenient way to parameterize the unresolved boundary layer in our class of eddy-admitting to eddy-resolving grids. For BB12, we experimented two different conditions, in addition to the free-slip condition used in Section 3.1: the no-slip condition (the tangential velocity vanishes at the coast, hereafter BB12_ns) and the partial-slip condition (the tangential velocity at the coast is set to half the offshore velocity, hereafter BB12_ps). Fig. 5 investigates the impact of these three formulations on the meridional current simulated in the southern Bay in March–April–May and October–November–December, during the poleward and equatorward seasons of the EICC, respectively. The chosen latitude (11°N) corresponds to the latitude of maximal seasonal variability of the boundary current (Durand et al., 2009). In March–April–May (Fig. 5(a)), we find again a good agreement between ORCA025 and BB12, which we had seen on Fig. 2. In ORCA025 (respectively BB12) the poleward EICC flows at 0.4 m s^{-1} (respectively 0.5 m s^{-1}) at 80.5°E just off the west coast, and decays rapidly eastward; at subsurface, it extends down to about 100 m (respectively 150 m), consistently in both simulations. This basic pattern is also seen in BB12_ps, with a coastal maximum at the same longitude, but with a magnitude and vertical extent slightly reduced. In the BB12_ns solution, the core of maximum current is displaced offshore, with values hardly exceeding 0.2 m s^{-1} in the upper 60 m. Similar conclusions can be drawn for the October–November–December situation, when the EICC flows equatorward: ORCA025 and BB12 simulate a coastal maximum of the current, with comparable magnitudes (0.5 m s^{-1}) and downward extent (about 170 m in ORCA025 and 120 m in BB12). In both BB12_ps and BB12_ns, the current is significantly slower (0.2 m s^{-1}) and extends to shallower depths (60 m). The available observations preclude a definite validation of the various simulations. However, both the ship drifts reported by Mariano et al. (1995) and the altimetry-derived currents of Durand et al. (2009) suggest that the surface EICC flows southward at speeds in excess of 0.6 m s^{-1} in October–November–December. This pleads for identifying BB12 as the most realistic of the three 1/12° runs. In March–April–May, it is hard to conclude anything, as the ship drifts suggest a northward EICC at 0.4 m s^{-1}, and the altimetry-derived currents hardly reach 0.25 m s^{-1}. The vertical extent of the boundary current is impossible to validate with the available data.

Beyond the magnitude of the boundary current, it is interesting to assess the impact of the sidewall parameterization on the meridional transport of the boundary current. Fig. 6 presents the longitudinal variation of the meridional transport, integrated over the upper 200 m, and integrated eastward from the western boundary, for March–April–May and October–November–December. By definition, it starts from a null transport at 80°E (the westernmost grid point); the value at 99°E (the easternmost grid point) represents the total (basin-wide) meridional transport (averaged on 2003–2006). In March–April–May, all simulations show a poleward western boundary current, with variable magnitude: it peaks at 5.5 Sv in BB12 and 4 Sv in both BB12_ps and BB12_ns. ORCA025 shows a lower value (2.5 Sv). In October–November–December, the contrast between the various simulations is even stronger: BB12 and ORCA025 exhibit a 3–3.5 Sv equatorward current at the western boundary, whereas BB12_ps and BB12_ns show hardly any boundary transport. Eastward of the western boundary regime, the scatter between the different simulations is strong in both seasons. The reason for this is not clear. The zonally integrated meridional transport from western boundary to eastern boundary (given by the easternmost value of the curves) is roughly consistent between the various simulations, around 2 Sv northward in both seasons.

The validation of modelled sea level led us to conclude that the 8 km grid of BB12 yields a realistic level of variability, unlike the 25 km grid of ORCA025. The sensitivity of the dynamics to the lateral momentum boundary condition is strong in BB12; based on the available current data (surface only), the boundary current simulated during winter in the free-slip formulation appears as the most satisfactory. In the remainder of this paper, we thus utilize this configuration (BB12, free-slip) to investigate the salinity structure of the Bay. However, the issue of choosing the boundary friction condition should be re-visited more systematically when long enough observational records of the western boundary current become available.

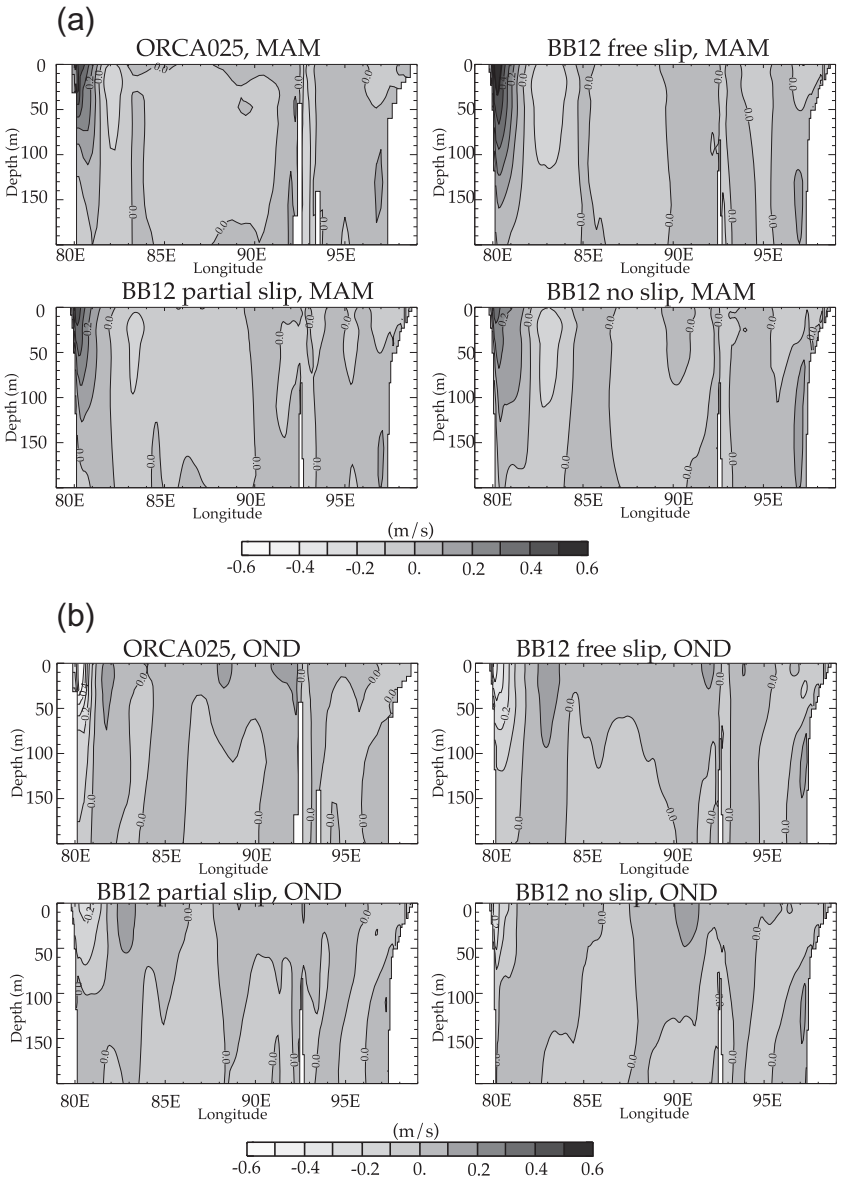

Fig. 5. (a) Longitude-depth section of the meridional current along 11°N simulated by ORCA025 and by BB12 (using the free-slip, partial-slip and no-slip sidewall boundary condition), for March–April–May. Isocontours are every 0.1 m s^{-1}. (b) Same as (a), for October–November–December.

4. Salinity response to the precipitation forcing flux

4.1. Precipitation products

The issue of salinity response to precipitation forcing over the tropical Indian ocean has already been investigated in a few modelling studies. Yu and McCreary (2004) used an OGCM over the tropical Indian Ocean, to determine the SSS response to six different precipitation products (in-situ only, satellite-only, merged satellite – in situ datasets and reanalysis products). They identified CMAP (Xie et al., 2007) as the product yielding the smallest biases in their modelled SSS at basin scale. However, their runs were significantly biased throughout the northern periphery of the Bay, due to a crude parameterization of the continental runoff. Based on the same numerical framework, and making use of a sophisticated data assimilation scheme, Yaremchuk (2006) attempted to retrieve an optimal precipitation field from the information contained in SSS observations. His approach, though promising, clearly suffered from the limited number of observations available at that time. Here we adopt an approach similar to that of Yu and McCreary (2004), based on the best numerical simulation we set up in the previous section. In particular our study benefits from a model with high resolution (on both the horizontal and the vertical), with sophisticated vertical physics, and with realistic runoff forcing. We consider four different precipitation products, representative of the state-of-the-art: 6-hourly ERA-Interim (henceforth ERAI; Dee et al., 2011), daily GPCP (Huffman et al. 2001), monthly DFS4 (Brodeau et al., 2010) and daily TMI (Wentz et al., 2000). ERAI is a reanalysis product, GPCP merges in situ and remote sensing datasets, DFS4 consists of a globally-balanced blend of GPCP (Adler et al., 2003) and CMAP (Xie et al., 2007) datasets, and TMI is a pure remote sensing product. The precipitation products are presented on Fig. 7. Basically all four products broadly agree in the yearly precipitation average of 4 to 6 mm per day at the scale of the basin, with a dry period (less than 2 mm per day on average) in February–March–April, a summer monsoon setting in during May–June–July,

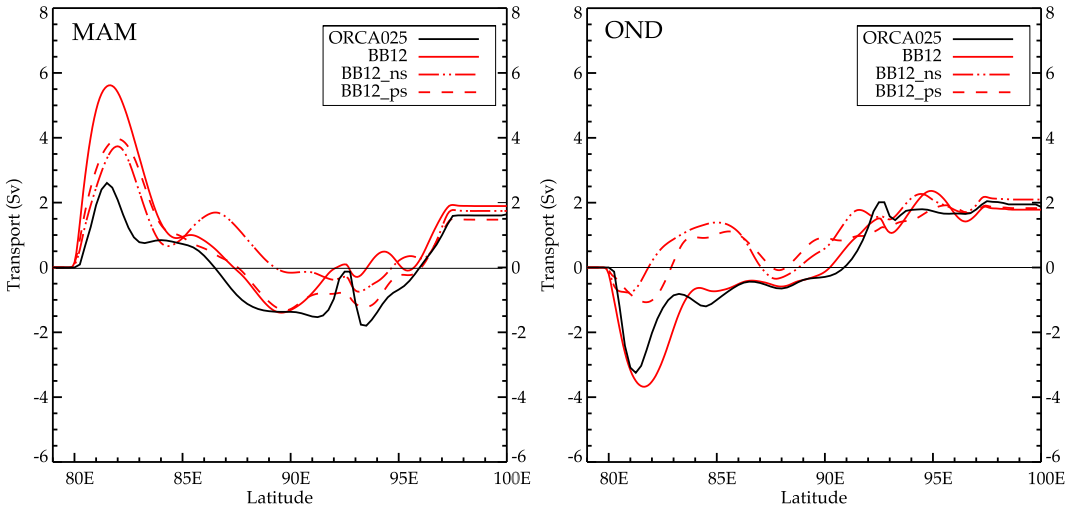

Fig. 6. 0–200 m meridional transport across 11°N integrated eastward from the western boundary, simulated by ORCA025 and by BB12 (using the free-slip, partial-slip and no-slip sidewall boundary condition), for March–April–May (left) and October–November–December (right).

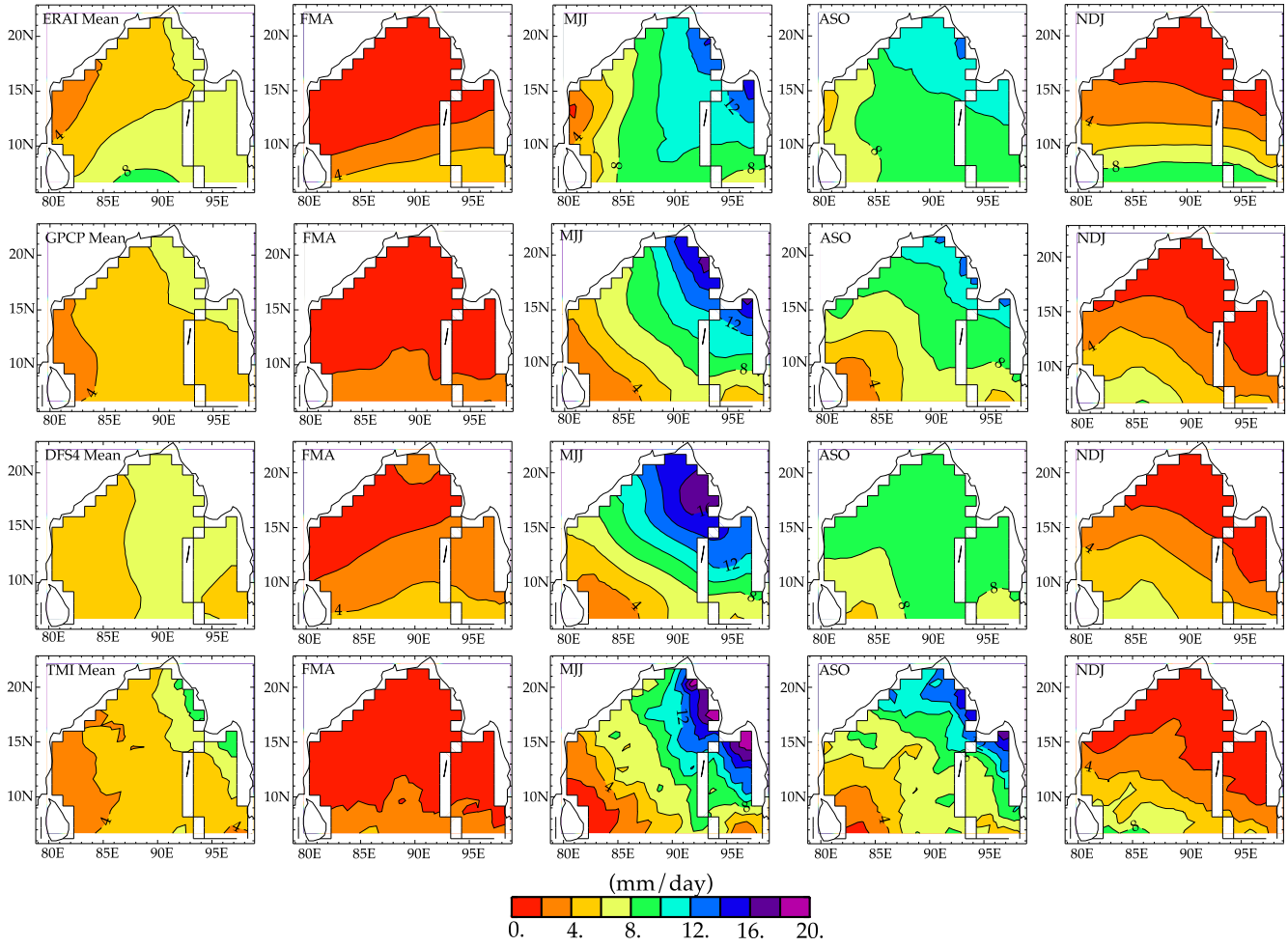

Fig. 7. Long-term mean (first panel) and quarterly (second to fifth panel) evolution of the precipitation flux, for ERAI, GPCP, DFS4 and TMI products, from first to fourth row respectively. Isocontours are every 2 mm/day.

decaying in August–September–October and again dry conditions in November–December–January. However strong local discrepancies appear among the various products: ERAI shows a maximum of the yearly average located at the southern edge of the basin (at 7°N), whereas TMI (and, to a lesser extent, GPCP and CMAP) show their maximum in the North-Eastern part of the basin. ERAI exhibits yearly mean values in excess of 6 mm/day all over the southern Bay, reaching 8 mm/day in a patch centered on (88°E,

6°N), whereas TMI remains between 4 mm/day and 6 mm/day. The excess precipitation in ERAI in the southern half of the basin is seen in all seasons.

4.2. SSS observations

The validation of SSS simulated in response to the various precipitation products is a key-step of our numerical study, as the SSS climatologies published so far (based on historical hydrographic data) suffer from considerable inaccuracies over the Bay (with typical errors of order 0.5 at basin scale, and in excess of 3 in the near-coastal regions during summer; Yaremchuk et al., 2005). We thus built an observed SSS climatology, comprising all the existing ARGO profiling float and ship-borne Conductivity-Temperature-Depth (CTD) data over the 1999–2008 period. Based on an approach similar to ours (by blending of ARGO data and historical CTD data), Thadathil et al. (2007) also worked out a climatology of SSS in the Bay, and published a sub-set of it (see their Fig. 5). Our product is essentially in line with theirs, except for the dataset from Indian Oceanographic Data Centre that were not available to us. For ARGO and CTD, SSS is defined as salinity taken at 10 m depth, to avoid surface pollution of the measurement. Argo network has reached its target density of observations of one profile every 300 km and 10 days in late 2006. The recent period hence provides a sufficient spatial and temporal coverage to provide SSS monthly estimates. SSS is estimated from individual measurements in each $1° \times 1°$ box, for each month of the climatological year. Only the "good" (quality flag equals to 1) and "probably good" (quality flag equals to 2) ARGO salinity measurements have been considered. Reduction of the data is done by taking the median of all measurements in each grid box. Fig. 8 (first row) presents the observed climatological annual mean (first column), and the quarterly means (second to fifth column). The spatio-temporal data coverage is also shown on Fig. 8. Basically, one can have confidence in the large-scale structure depicted from the observations, for each of the four quarters (over most of the domain, the number of individual measurements used in each grid cell is typically superior to five). Our SSS product is thus appropriate to describe the seasonal evolution of SSS at basin-scale. However, one has to keep in mind that the available dataset leaves the shelf areas poorly monitored (number of measurements per pixel and per quarter inferior to three), with some extended areas not monitored at all. This is particularly the case throughout the Andaman Sea (to the East of 94°E). This legitimates our decision not to attempt any kind of extrapolation or gridding of this discontinuous product, for the reason that the SSS contrasts in these coastal areas are potentially high, and the data gap filling is thus hazardous. Over the region that is satisfactorily monitored by the available observations (typically: the entire basin situated to the South of 18°N and to the West of 93°E), the mean observed SSS field shows a contrasted pattern, with fresh waters (salinity lower than 33) in the north-eastern Bay, and saltier waters in the central and southern basin. This large-scale gradient is seen in all seasons, with some modulation. During the pre-summer monsoon season (MJJ) the freshwaters are restricted to the far north-eastern Bay (to the North of 13°N and to the East of 88°E). With the progress of summer monsoon (ASO), they migrate southward along both the eastern and western boundaries, with clear signatures along the East coast of India at 16°N, and in the Southern Andaman Sea. This is consistent with both western and eastern boundary currents flowing equatorward at the surface in the northern Bay, during this season (Shankar et al., 2002). The surface water also freshens in the northern Bay, with a minimum of 30 around (19°N, 90°E). This corresponds to both runoff (Papa et al., 2010) and oceanic precipitation (Hoyos and Webster, 2007) reaching their yearly maximum there. In contrast, there is an inflow of saltier water (in excess of 34) in the South-Western basin, consistently with the Summer Monsoon Current flowing eastward and thus conveying Arabian Sea High Salinity Water into the Bay. In Fall (NDJ) the fresh waters further propagate southward along the western boundary, with values inferior to 33 throughout the $(14°N–17°N) \times (82°E–87°E)$ area, and isolated pockets of fresh waters seen as far South as 8°N along the East coast of Sri Lanka. The evolution of salinity in the Andaman basin is not resolved by the available observations. During winter (FMA), the EICC turns poleward and we observe a northward retreat of the fresh waters in the western half of the basin, whereas the central basin (from 86°E to the Andaman arquipelago) shows a further decrease of SSS between 10°N and 14°N. In the north-eastern basin, the extremely fresh values (lower than 31) have disappeared. In the South-western corner, the Winter Monsoon Current flows westward and has pushed back the saltier Arabian Sea waters out of the Bay. The seasonal evolution seen in our product is basically consistent with the past literature published with the historical databases (e.g. Rao and Sivakumar, 2003), but we benefit from a significantly increased data coverage, that reveals much finer details of the field.

4.3. Simulated SSS

SSS from the four different simulations is presented on Fig. 9. Just like in the observations, the modeled SSS is in fact taken as the salinity simulated at 10 m depth. In general, it is hardly

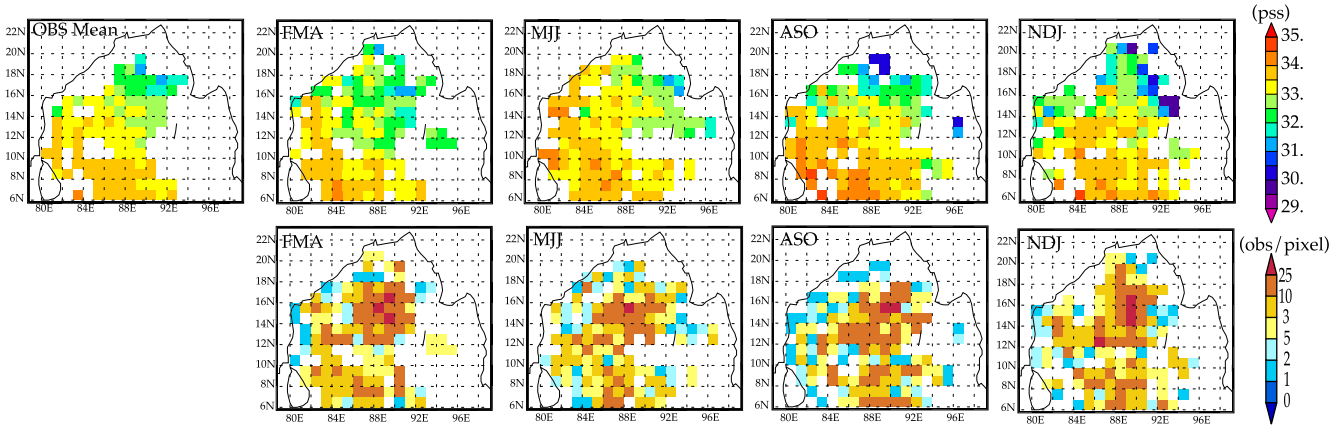

Fig. 8. Long-term mean (first column) and quarterly climatological (second to fifth column) evolution of observed SSS. First row shows the SSS, second row shows the corresponding data distribution (in number of observations per pixel and per quarter).

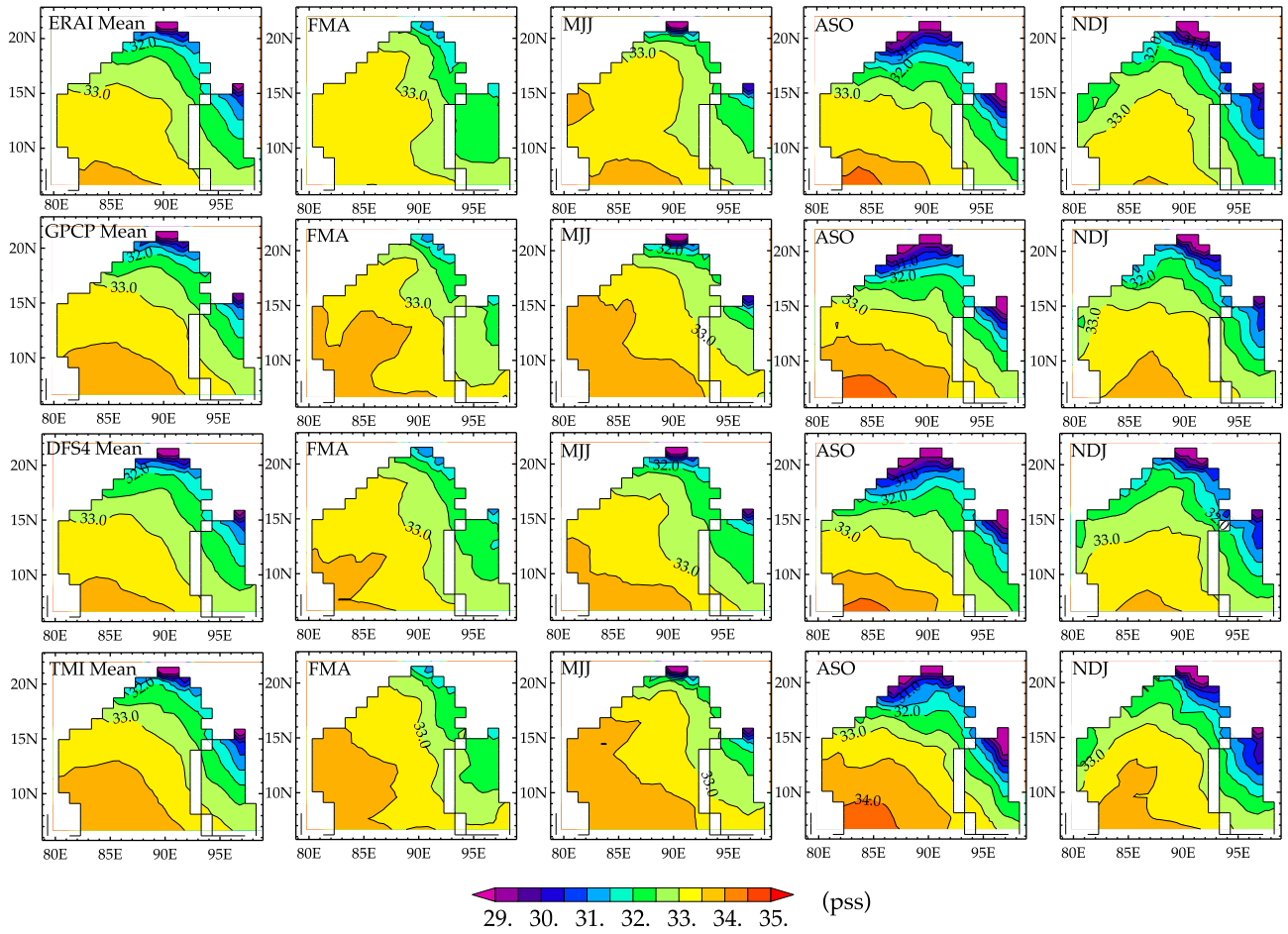

Fig. 9. Long-term mean (first column) and quarterly climatological (second to fifth column) evolution of SSS simulated by BB12. BB12 is forced by ERAI, GPCP, DFS4 and TMI precipitation flux, from first to fourth row respectively. Isocontours are every 0.5.

distinguishable from the true model SSS (not shown). For consistency, the native 1/12° fields were re-gridded on the 1° observational grid presented on Fig. 8. In a mean, all four simulations successfully capture the SSS of the two water masses co-existing in the Bay, as well as the North-West – South-East orientation of the front separating them. However, we can clearly see differences in the absolute values of simulated SSS: ERAI-forced simulation is hardly capable of producing waters saltier than 33.5 in the South-Western Bay, whereas TMI-forced run shows a 33.5 isohaline reaching 13°N in the central basin, just like in the observed field. GPCP and DFS4 runs exhibit an intermediate behaviour, with a fresh bias in the South-West but not as strong as in the ERAI run. This fresh bias in the ERAI-forced simulation mirrors the area of strong precipitation seen in the mean field (Fig. 7) and discussed in Section 4.1. Table 3 summarizes the validation of modelled SSS. It confirms that ERAI run has a predominantly fresh bias. The bias, however, remains inferior to 0.1 (in absolute values) for all four simulations. We supplemented our assessment of model SSS by comparing the various simulations with salinity recorded by one particular ARGO float, which identification number is 2900107. This float is remarkable, in that it was deployed in the central Bay in 2004, and was still active in 2012. In 2004–2006 (our period of interest), it has been drifting in the South-Western Bay, in the area [8°N–15°N] × [80°E–87°E]. This comparison confirmed that ERAI-forced simulation has a predominantly fresh bias (−0.16), superior (in absolute values) to the bias in DFS4-forced run (−0.05) and in TMI-forced run (+0.07). This comparison also confirmed that GPCP-forced run shows a positive bias (+0.18), even stronger (in absolute values) than the ERAI-forced run.

Table 3
(Model-observation) bias and standard deviation for the various simulations (forced by ERAI, GPCP, DFS4 and TMI precipitation product), for salinity at 10 m depth, with respect to the observed product. The modeled monthly climatological fields have been interpolated on the (gappy) observed grid for this computation.

Precipitation used	ERAI	GPCP	DFS4	TMI
Salinity bias	-9.7×10^{-2}	7.5×10^{-2}	-8.5×10^{-2}	8.57×10^{-2}
Standard deviation	0.61	0.60	0.60	0.58

Fig. 10 shows the distribution of model-data SSS difference, as a function of observed value. We present it for the simulation forced by TMI precipitation only, as the results are basically the same for the other runs (not shown). The dataset is the gridded field presented in Section 4.2. The model has a tendency to over-estimate the fresh salinities (typically inferior to 33), and to slightly under-estimate the higher salinities (above 33.5). Hence the model produces a too weak salinity contrast between Northern BoB fresh waters and saltier Arabian Sea waters. The typical value of the bias is inferior to or of order 0.5 in the range [32.5, 33], which is remarkably low compared to state-of-the-art OGCM simulations of the Bay (see e.g. Sharma et al., 2010, their Section 5).

4.4. Mixed-layer depth

Salinity is known to limit the thickness of the mixed layer in the Bay (e.g. Shenoi et al., 2002; Thadathil et al., 2002). It appears

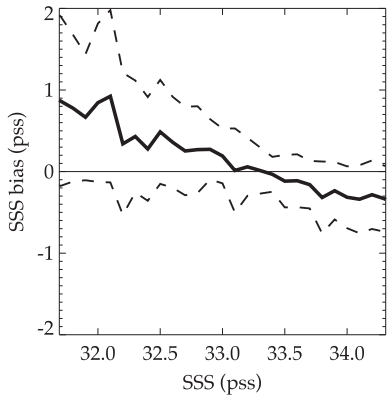

Fig. 10. Binned mean of SSS difference (model minus observations). The model run is forced by TMI precipitation. The upper and lower curves represent ±1 standard deviation. The bins are of 0.1 pss.

interesting to assess whether or not the differences seen in SSS among the various runs influence the mixed layer depth (MLD) simulated by the model. Fig. 11 presents the climatological MLD (in yearly mean and for four selected months, January, April, July and October) based an of updated version of the product of de Boyer Montégut et al. (2004) with ARGO data (first row) and simulated by the four runs (second to fifth row). For both the observations and the simulations, MLD is defined as the depth where density exceeds the density at 10 m depth by a value equivalent to a 0.2 °C decrease in temperature (see de Boyer Montégut et al. 2004 for full details on this choice of criterion). The observed MLD product, just like the SSS product introduced previously, is based on ARGO and CTD data. The mean field shows a bowl-like pattern, with thickest mixed layer (in excess of 30 m) in the central Bay, and shallower mixed layer (around 20 m) along the western and northern boundaries. The seasonal evolution shows a prominent semi-annual signal throughout the central basin, with maximum MLDs during both monsoons (January and July), and minimum MLDs in the intervening seasons. This suggests that the wind forcing (through turbulent mixing and/or through its effect on latent heat loss) is the main driver of the seasonal variability of MLD. In the Northern basin, where SSS is extremely low (Figs. 8 and 9), MLD variability is weaker (with a moderate deepening of the mixed layer during summer monsoon).

The MLD simulated by the model hardly depends on the precipitation forcing product, as all the four runs basically show a similar mean structure and similar seasonal evolution. They are all successful in capturing the bowl-like pattern, with deepening of the mixed layer in the central basin during summer monsoon and during winter monsoon, and shoaling in the post-monsoon seasons. The quantitative agreement between model and observations is remarkable, particularly during spring, summer and fall. In winter, the model overestimates the MLD by about 20 m in the center of the Bay (around 15°N, 88°E).

We have seen that a careful choice of the precipitation product is a must to simulate a realistic SSS over the Bay. In this regard, TMI appears as the best product among the four ones we tested. The worst product appears to be ERAI, in that excess precipitation in the southern half of the basin induces a fresh bias there. The seasonal cycle of simulated SSS, however, is consistent between the four simulations. The MLD simulated by the model does not appear to be sensitive to the choice of the precipitation product, with equally good performance of all four simulations.

Apart from the thin mixed layer, the Bay of Bengal is also characterized by the frequent presence of a salinity-mixed layer shallower than the temperature mixed-layer. The layer stratified in salinity, separating the upper mixed layer from the thermocline, is termed as the barrier layer (Lukas and Lindstrom, 1991). The barrier layer is known to appear seasonally in the north-eastern Bay during summer monsoon, then to spread westward and southwestward (along the western boundary) during the post-monsoon season; it eventually decays during spring (Mignot et al., 2007; Thadathil et al., 2007). The barrier layer, being stably stratified in salinity, can support the existence of a temperature inversion (e.g. Thadathil et al., 2002; Durand et al., 2004). The northern half of the Bay of Bengal typically shows consistent temperature inversions of up to 1 °C during winter, in the periphery of the basin; the southern and central part of the basin (where barrier layer is thin or absent) hardly ever shows significant temperature inversions (Thadathil et al., 2002). The model was found to successfully simulate the observed seasonal patterns of barrier layer thickness and temperature inversion (see https://www.locean-ipsl.upmc.fr/~rblod/Upper_BoB_Sal/index.html for the model maps of barrier layer thickness and temperature inversion).

5. Freshwater export pathways: a passive tracer approach

The freshwater received by the Bay consists of oceanic precipitation (5900 km^3/year for the TMI product) and runoff from a couple of mighty river systems (1000 km^3/year for the Ganges–Brahmaputra system, 400 km^3/year for the Irrawaddy; Dai and Trenberth, 2002). From Fig. 7, it appears clearly that the area of maximum oceanic precipitation is located in the north-western Bay. There, the precipitation is mostly concentrated during summer monsoon (see Fig. 7 and Hoyos and Webster, 2007). Averaged on a box (88°E–94°E) × (14°N–23°N), the oceanic precipitation cumulated from 1st June to 31st August represents 75% of the total yearly precipitation. As for runoff, Ganges–Brahmaputra and Irrawaddy also concentrate most of their contribution during this June–August period (67% of the yearly total for the Ganges–Brahmaputra, and 69% of the yearly total for Irrawaddy).

In this section, our objective is to use our model to identify the fate of the freshwater, once it has been accumulated in the Northern Bay during the summer monsoon. This issue has already been investigated in the past, based on in situ observations (Shetye, 1993) and on coarse resolution models (Jensen, 2001, 2003; Vinayachandran and Kurian, 2007; Durand et al., 2011). Our approach is based on passive tracer experiments, integrated on line (using exactly the same physics and numerics as for temperature and salinity) that will allow us to distinguish between the various sources of freshwater. To do so, we defined three different tracers in our BB12 model: one that traces the continental freshwater originating from the Ganges–Brahmaputra system (noted "GB tracer"), one representing the continental freshwater originating from the Irrawaddy (noted "Ir tracer"), and one for the oceanic precipitation falling in the box (88°E–94°E) × (14°N–23°N) (noted "OP tracer"). Each tracer is injected in the model on September 1st uniformly over each of the three boxes over which the freshwater has been accumulated from June to August (visible on Fig. 12, 1st row). The quantity of tracer is chosen so that the concentration of tracer in the mixed layer can be interpreted as an equivalent of the concentration of fresh water accumulated during June–July–August, in the mixed layer. The initial quantity is thus equal the amount of freshwater received by the ocean from each of the three sources considered, over the (1st June–31st August) period: 15100 kg m^{-2} for GB tracer, 9300 kg m^{-2} for Ir tracer, and 1700 kg m^{-2} for OP tracer. The tracers can thus be simply considered as quantitative markers of the three different freshwater masses accumulated in the mixed layer in the northern Bay at the end of summer.

As an example, Fig. 12 illustrates the time evolution of each of the three tracers, for an experiment started on September 1st 2003. In this figure, tracers concentrations have been integrated

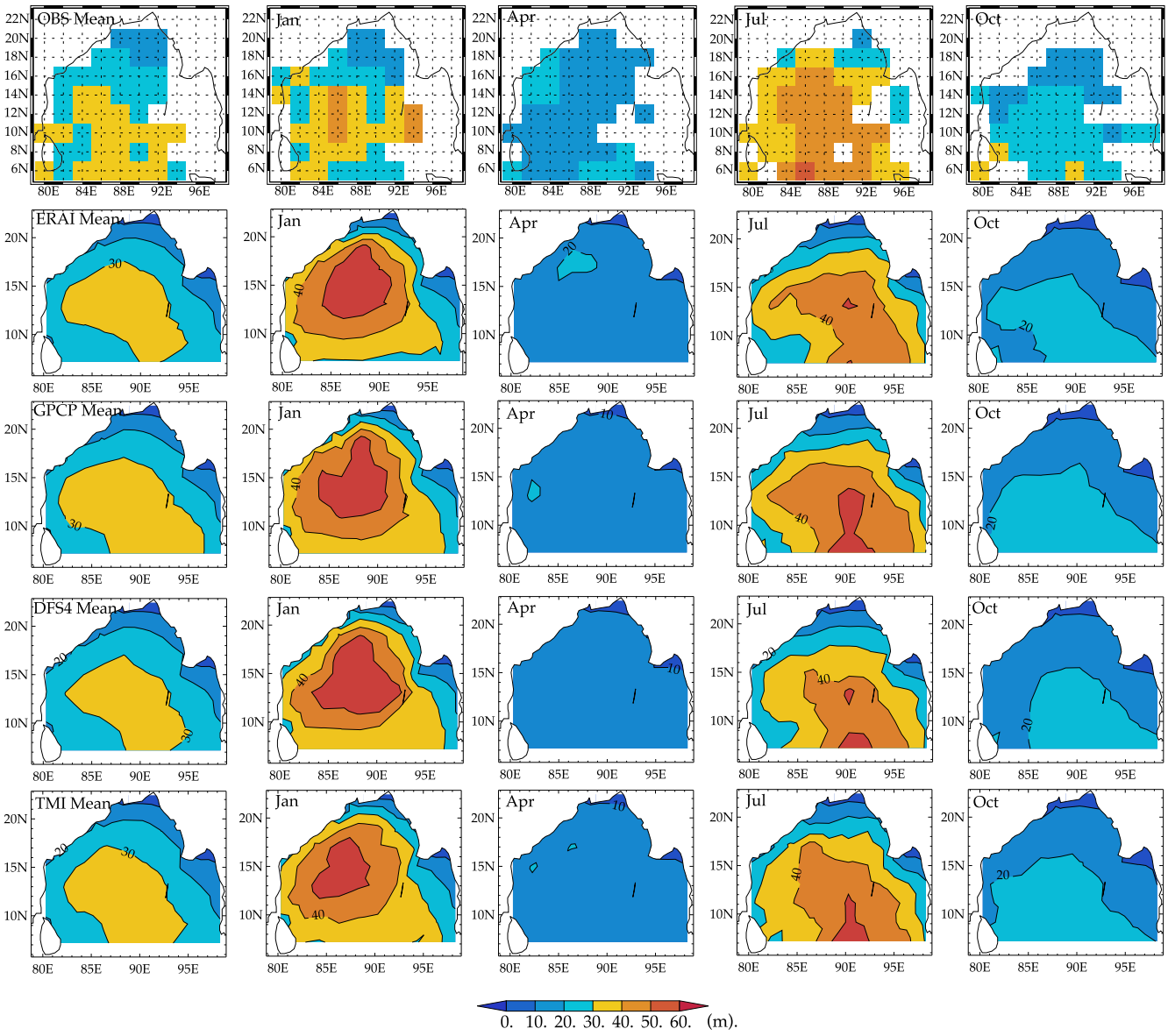

Fig. 11. Long-term mean (first column) and monthly climatological (second to fifth column) evolution of MLD, as observed (first row) and simulated by BB12 (second to fifth row). BB12 is forced by ERAI, GPCP, DFS4 and TMI precipitation flux, from second to fifth row respectively. The colorbar is the same for observed and modelled fields. For modelled fields, isocontours are every 10 m.

over the mixed layer, so that the maps feature contours with units kg m^{-2}. Basically, the evolution of GB tracer plume in 2003 mimics the (limited) in situ SSS observations reported by Shetye (1993), with an offshore spreading in the Northern Bay in September–October, followed by a rapid export as a narrow tongue hugging the western boundary around December. In contrast with Shetye (1993), however, GB tracer does not spread in the open Bay just after monsoon. Rather, it enters the northern central basin as a thin filament emerging from the Western boundary as far south as 16°N, and retroflecting eastward. A comparable evolution is seen in the 2004 and 2005 experiments (not shown). As an example, an animation of the GB tracer evolution is available on https://www.locean-ipsl.upmc.fr/~rblod/Upper_BoB_Sal/index.html. A similar discrepancy was noted by Vinayachandran and Kurian (2007) when comparing the freshwater plume observed during BOBMEX cruises and simulated by their eddy-admitting model, with the model overestimating the southward extent of the freshwater plume. In our high-resolution experiments, it appears quite clearly that the meso-scale features play a key-role in trapping the freshwater in the Northern basin.

Fig. 13 presents a systematic assessment of the role of each of the three sources in the wintertime export of freshwater from the Northern Bay to the Southern Bay. It displays the seasonal climatology of the longitude-time distribution of each of the three freshwater masses (and their combination) in the central basin (at 11°N). It is expressed in terms of equivalent freshening (in PSS) induced by the amount of freshwater contained in the mixed layer, for each of the three freshwater masses. This quantity is simply inferred from the dilution equation:

$$\text{equivalent freshening} = \frac{S_{ML} \times H}{MLD} \tag{1}$$

where S_{ML} is the salinity averaged over the mixed layer (in PSS), H is height of the remaining fresh water originating from the northern Bay computed from the tracer content of the mixed layer multiplied by 1000 (the density of fresh water) and MLD is the mixed layer

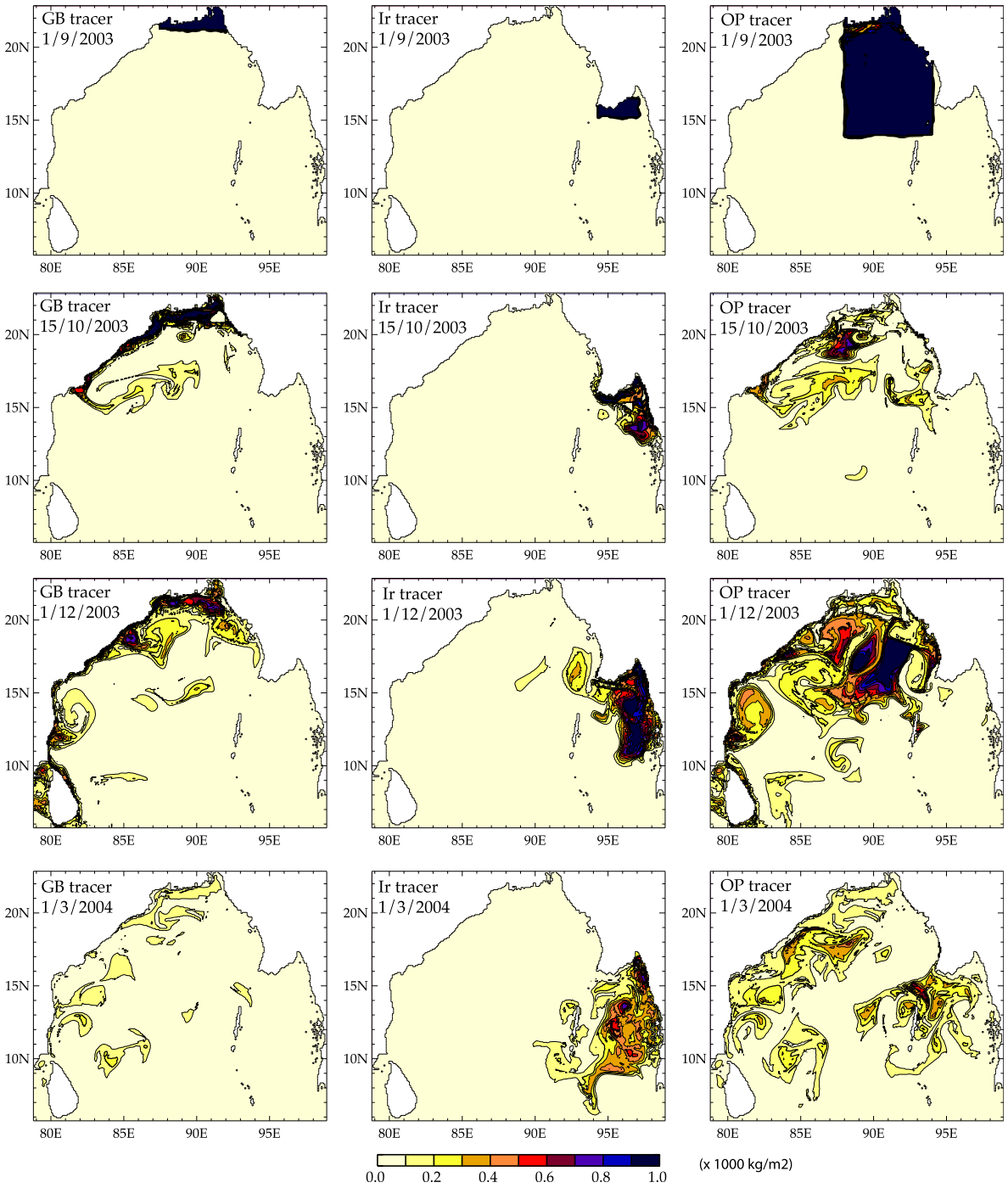

Fig. 12. Evolution of the passive tracer concentration (averaged over the mixed layer) for (left column) GB tracer, (centre column) Ir tracer, and (right column) OP tracer. The snapshots are taken from the first experiment carried out (over 2003–2004). First row (1/9/2003) is the day of the tracer release. Second, third and fourth row correspond respectively to 45 days, 90 days and 180 days later. The unit is equivalent to tons of freshwater per meter square (see the text for details). Isocontours are every 0.1.

depth (in m). The top left panel features the total contribution of the three freshwater masses. It is seen that they do not invade uniformly the basin, consistently with what was seen on Fig. 10. Rather, the freshwater signature is confined to both eastern and western boundaries, and appears there almost simultaneously in late October (western boundary) - early November (eastern boundary). The western boundary shows a freshening confined shoreward of 82°E (about 200 km wide in the cross-shore direction), lasting about 3 months, whereas the pattern at the eastern boundary is wider (500 km) and lasts longer (more than 5 months). Both bursts typically consist of a 0.5 to 0.7 pss drop of the mixed layer salinity at their peak (mid-November to mid-December at 80°E, late November to late January at 97°E). It is thus seen that this freshening explains most of the overall SSS drop seen at both boundaries from monsoon to post-monsoon season (Fig. 7). The top right, bottom left and bottom right panels of Fig. 13 present the individual contribution of OP, GB and Ir freshwater masses, respectively. It is seen that the western boundary freshening is roughly equally driven by GB and OP water masses (each of them inducing a 0.3 salinity drop between 80°E and 81°E, in November). In contrast, the eastern boundary freshening is mainly generated by Ir water mass (with marginal contribution of OP water mass); in particular, this implies the

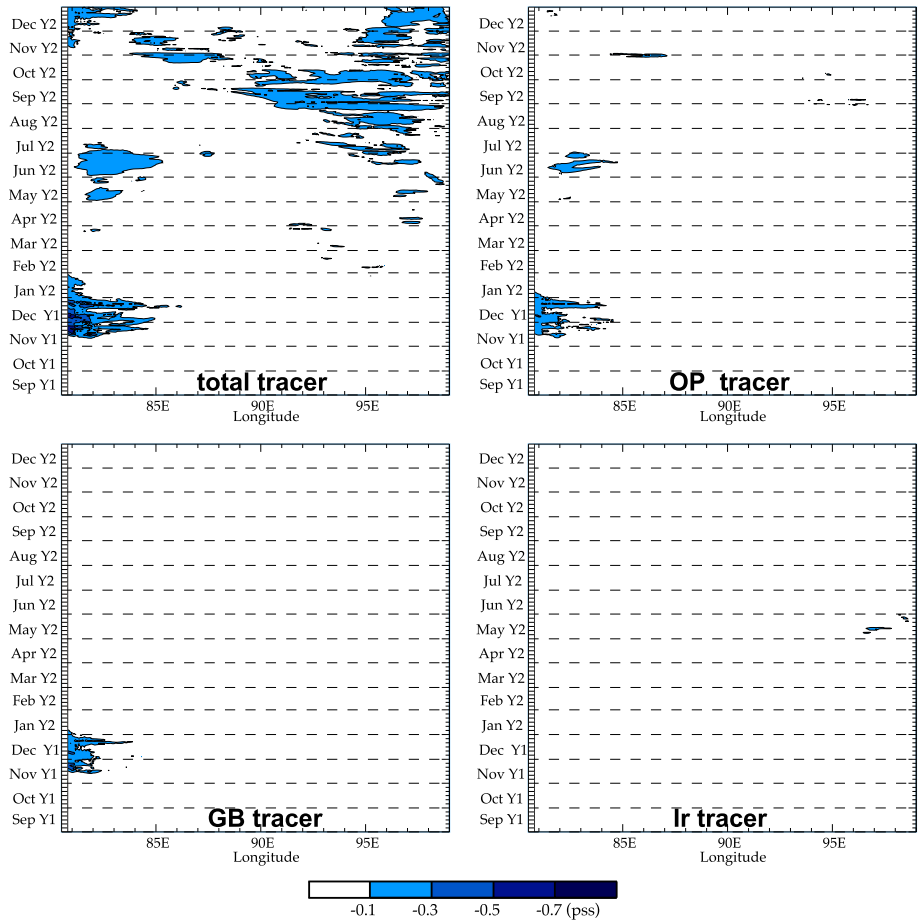

Fig. 13. Longitude-time evolution of the mixed layer freshening induced by the water masses tagged by the three passive tracers, along 11°N; top left is for the sum of the three tracers, top right is for OP tracer, bottom left is for GB tracer, and bottom right is for Ir tracer. The plotted field corresponds to the average of the three tracer experiments carried out (2003–2004, 2004–2005 and 2005–2006) and encompasses 16 months (from September of first year to December of the second year). Isocontours are every 0.2.

inability of Ganges–Brahmaputra waters to enter the Andaman Sea (a semi-enclosed basin, as seen on Fig. 1). Fig. 14 presents the same quantity as on Fig. 13, at the southern exit of the Bay (along 6°N). At the western boundary, a similar evolution is seen at 6°N as the one seen at 11°N, though with a 15 days delay (consistent with the southward travel time of the freshwater tongue). The freshening magnitude, however, is significantly reduced at 6°N as compared to 11°N (0.3 to 0.5 pss total, composed of a 0.1 to 0.3 pss contribution of OP and GB water masses). In the eastern basin, in contrast, the signature of Irrawaddy waters is not seen at 6°N, hereby suggesting that this water mass gets dissipated en route in the Andaman Sea. The decrease of the magnitude of the freshening (at the western boundary) or its disappearing (in the Andaman Sea) from 11°N to 6°N is explained by the vertical export of freshwater. This vertical export of freshwater is illustrated by Fig. 15, for the dominant source of freshwater (OP tracer). It displays the climatological temporal evolution of the vertical structure of the tracer plume from its release date (September 1st), averaged over the area that retains most of it in the Northern Bay (84°E–94°E) × (18°N–23°N). One can see a rapid export of the tracer from the surface downwards, through the base of the mixed layer and into the pycnocline. It occurs over timescales of a few weeks, with a 50% decrease of the tracer concentration reached by early October. This is certainly driven by the vertical mixing in the model. The decrease in tracer concentration in the mixed layer persists through January–February, when the concentration has been divided by about 10.

Our conclusion that the signature of the freshwater tongue gets gradually eroded from its origin in the Northern Bay to the Southern exit of the basin is in line with the conclusions we drew with a coarse version (0.5°) of our model (Durand et al., 2011), where we concluded that year-to-year anomalies of GB inflow hardly make their way to the Southern tip of Sri Lanka. This is also consistent with the study of Han and Webster (2002), who assessed the impact of interannual variability of G-B runoff on the Bay sea level variability, also in a 0.5° resolution OGCM. They used a completely different model, with a rather coarse vertical resolution, with a completely different vertical physics from ours. They forced the SSS of their model with a synthetic river runoff product, essentially extrapolated from the variability of continental rainfall over the G-B watershed, over the period 1958–1998. Their GB runoff time serie exhibited a marked year-to-year variability. One of their conclusions was that their simulated sea level south of 16°N along the western boundary of the Bay is hardly impacted by the interannual variability of the river runoff. This is in line with our own conclusion, and thus suggest that the horizontal resolution of the model grid is not responsible for the propensity of the models to retain the imprint of salinity anomalies in the Northern Bay during the year following their genesis. To check this, we carried out a similar passive tracer integration in ORCA025 model. The pathways and circulation timings are in line with our conclusions for BB12 and with the past findings of Han and Webster (2002) and Durand et al. (2011) (not shown). One difference, though, is that the magnitude of the freshening plume propagating along the western boundary during the post-monsoon season is about twice stronger in ORCA025 compared to BB12. This may be explained by the more intense horizontal exchanges between the western

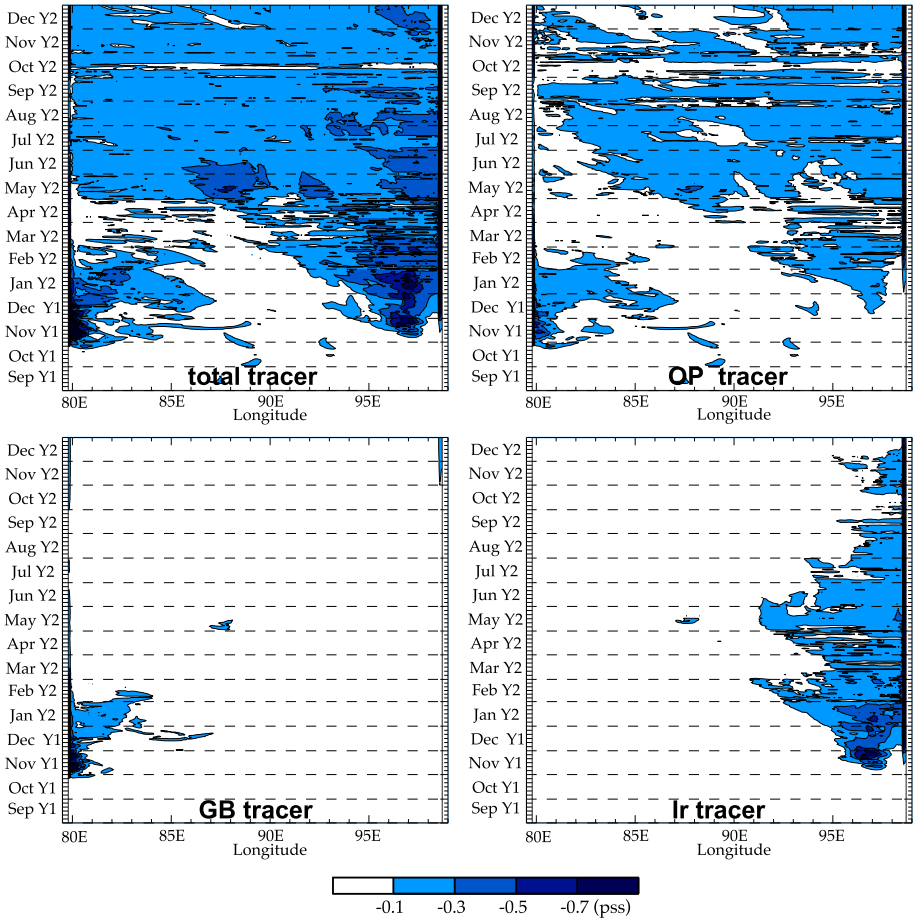

Fig. 14. Same as Fig. 13, along 6°N.

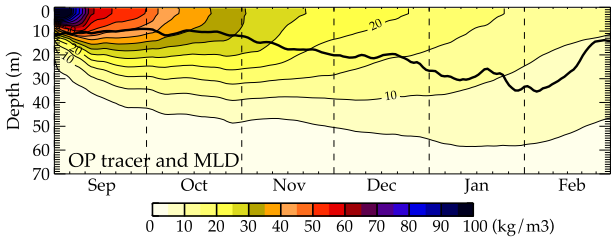

Fig. 15. Depth-time evolution of OP passive tracer averaged over the northern Bay (84°E–94°E × 18°N–23°N). The plotted field corresponds to the average of the three tracer experiments carried out (2003–2004, 2004–2005 and 2005–2006) and encompasses 6 months (from September of first year to February of the second year). Isocontours are every 5 kg m^{-3}. Superimposed (solid) is the evolution of the mixed layer depth.

boundary and the basin interior in BB12, driven by stronger mesoscale recirculations, that act to "drain" the coastal freshwater plume more efficiently.

The rapidity of the vertical export of surface tracer seen in our model is surprising, based on the widespread belief that the upper layer of the Bay of Bengal exports its freshwater predominantly via horizontal transports rather than via vertical mixing (e.g. Jensen, 2001, 2003; Gopalakrishna et al., 2005). This said, we are rather confident in the model physics, given the excellent quality of the SSS field it simulates. Clearly, this calls for dedicated in situ measurements of the vertical exchanges in this part of the basin, to identify the physical mechanisms responsible for the vertical export.

6. Concluding remarks

In this study, we make use of various versions of the NEMO model to simulate the upper ocean circulation and salinity structure in the Bay of Bengal. Our primary objective is to illustrate and quantify the sensitivity of the model response to three different kinds of model settings: the horizontal resolution, the sub-grid scale parameterizations and the forcing fluxes at air-sea interface. We first compare two different resolutions of our model, with 1/4° and 1/12° grids. The 1/4° version is eddy-admitting, and essentially fails to reproduce the observed level of sea surface height variability. In contrast, the 1/12° version is eddy-resolving, and successfully simulates it. Given the central role played by horizontal circulation in the structure of the salinity in the Bay, this conclusion has strong implications for the future modeling efforts in this part of the world ocean. To illustrate the effect of sub-grid scale numerical parameterizations, we show that a careful choice of the sidewall boundary condition has to be made to ensure a realistic simulation the circulation simulated. In our case, the free-slip condition yields the most realistic western boundary current, while the no-slip condition virtually kills its transport. The impact of the atmospheric forcing products on the ocean model skills is finally investigated, through comparisons between four runs forced by four different precipitation products. Expectedly, sea surface salinity appears sensitive to the precipitation product used to force the model. ERAI (Dee et al., 2011) yields excess summer monsoon precipitation in the southern Bay, hereby generating a fresh bias there. The various spaceborne precipitation products we tested perform significantly better.

After having completed and assessed the set-up of our model, we then investigated the kinematics of the freshwater plume emanating from the Northern Bay during summer monsoon. Our experimental approach (tagging of model water masses with three distinct passive tracers) allowed us to distinguish between the three main components of the Northern Bay freshwater plume, which are oceanic precipitation, Ganges–Brahmaputra waters and Irrawaddy waters. Our main finding is that oceanic precipitation as well as Ganges–Brahmaputra waters get exported to the southern Bay (as far South as 6°N, viz. at the southern tip of Sri Lanka) via the western boundary of the basin, with comparable contribution of the two freshwater sources; in contrast, Irrawaddy waters remain trapped in the northern half of the Andaman basin. The freshwater plume gets gradually eroded in its southward journey, as it gets mixed with the underlying saltier layer by the vertical exchanges. Gopalakrishna et al. (2005) sought the origin of observed year-to-year South Eastern Arabian Sea salinity anomalies in the Bay precipitation and runoff conditions during the preceding season. Our passive tracers experiments confirm that this connection exists, with equal contribution of Ganges–Brahmaputra outflow and of precipitation falling over the northern Bay.

Our experiments suggest that the vertical exchanges of mass between the upper mixed layer and the pycnocline layer play a central role in the fate of the freshwater plume. One of the limitations of our modeling framework is the absence of parameterization of tidal mixing in our model. Indeed this process is known to drive intense vertical mixing in some parts of the world ocean (e.g. Koch Larrouy et al., 2006). This issue certainly deserves further research effort, as proper implementation of this process is not straightforward.

Concerning the resolution of the model, we have seen that the transition from 1/4° to 1/12° induces a profound change in the level of variability of the upper circulation. The detailed investigation of the effects of this different circulation variability on the oceanic tracers pathways and water masses transformations will form the focus of a future paper. With the advent of high-performance computing systems, it will soon be possible to investigate the impact of higher resolution on the realism of the modeled circulation. Submesoscale dynamics are indeed known to exert a strong control on the large-scale vertical physics (e.g. Lévy et al., 2012, and references therein), and thus have the potential to alter our description of the fate of the Bay freshwater described in the present paper.

Our last remark concerns the climatic impact of salinity in the Bay. The extremely strong salinity stratification is responsible for the consistently high SSTs throughout the basin (Shenoi et al., 2002; de Boyer Montégut et al., 2007). Due to this high background state, the SST variability has the potential to profoundly influence the overlying atmosphere, over a broad range of timescales (e.g. Vecchi and Harrison, 2002; Vinayachandran et al., 2012). With the present study, we provide a realistic, quantitative oceanic component that paves the way to tackle this issue in a coupled framework.

Acknowledgments

Financial support for this work was provided by the GMMC (Groupe Mission MERCATOR/CORIOLIS). The computations were conducted with support of IDRIS/CNRS, the physical model was provided by the NEMO system (www.nemo-ocean.eu). The altimeter products were produced by Ssalto/Duacs and distributed by Aviso, with support from CNES (http://www.aviso.oceanobs.com/duacs/). TMI data are produced by Remote Sensing Systems and sponsored by the NASA Earth Science MEaSUREs DISCOVER Project. Data are available at www.remss.com. The Argo data were collected and made freely available by the International Argo Program and the national programs that contribute to it (http://www.argo.ucsd.edu, http://argo.jcommops.org). The Argo Program is part of the Global Ocean Observing System.

Appendix A. Supplementary data

Supplementary data associated with this article can be found, in the online version, at http://dx.doi.org/10.1016/j.ocemod.2013.12.001.

References

Adler, R.F., Huffman, G.J., Chang, A., Ferraro, R., Xie, P., Janowiak, J., Rudolf, B., Schneider, U., Curtis, S., Bolvin, D., Gruber, A., Susskind, J., Arkin, P., Nelkin, E., 2003. The version 2 global precipitation climatology project (GPCP) monthly precipitation analysis (1979-Present). J. Hydrometeor. 4, 1147–1167.

Blanke, B., Delecluse, P., 1993. Low frequency variability of the tropical Atlantic ocean simulated by a general circulation model with mixed layer physics. J. Phys. Oceanogr. 23, 1363–1388. http://dx.doi.org/10.1175/15200485.

Bourdalle-Badie, R., Tréguier, A.-M., 2006. A climatology of runoff for the global ocean-ice model ORCA025. Mercator-Ocean Report, MOO-RP-425-365-MER.

Brodeau, L., Barnier, B., Tréguier, A.-M., Penduff, T., Gulev, S., 2010. An ERA40-based atmospheric forcing for global ocean circulation models. Ocean Modell. 31 (3–4), 88–104. http://dx.doi.org/10.1016/j.ocemod.2009.10.005.

Chelton, D., Roland, B., deSzoeke, B., Schlax, M.G., El Naggar, K., Siwertz, N., 1998. Geographical variability of the first baroclinic rossby radius of deformation. J. Phys. Oceanogr. 28, 433–460, http://dx.doi.org/10.1175/1520-0485(1998)028<0433:GVOTFB>2.0.CO;2.

Dai, A., Trenberth, K.E., 2002. Estimates of freshwater discharge from continents: latitudinal and seasonal variations. J. Hydrometeorol. 3, 660–687.

de Boyer Montégut, C., 2005. Couche mélangée océanique et bilan thermohalin de surface dans l'Océan Indien Nord (PhD thesis). University of Paris VI, 181pp. Available on: tel.archives-ouvertes.fr/docs/00/05/58/75/PDF/these_clem_pdf_edition_20051025.pdf.

de Boyer Montégut, C., Madec, G., Fischer, A.S., Lazar, A., Iudicone, D., 2004. Mixed layer depth over the global ocean: an examination of profile data and a profile-based climatology. J. Geophys. Res. 109, C12003. http://dx.doi.org/10.1029/2004JC002378.

Dee, D.P. et al., 2011. The ERA-interim reanalysis: configuration and performance of the data assimilation system. Q. J. R. Meteorol. Soc. 137, 553–597. http://dx.doi.org/10.1002/qj.828.

Denis, B., Côté, J., Laprise, R., 2002. Spectral decomposition of two-dimensional atmospheric fields on limited-area domains using the discrete cosine transform (DCT). Mon. Weather Rev. 130, 1812–1829.

Diansky, N.A., Zalesny, V.B., Moshonkin, S.N., Rusakov, A.S., 2006. High resolution modeling of the monsoon circulation in the Indian Ocean. Oceanology 46, 608–628.

Drakkar Group, 2007. Eddy-permitting ocean circulation hindcasts of past decades. CLIVAR Exchanges 42, 12 (3), 8–10.

Durand, F., Shetye, S.R., Vialard, J., Shankar, D., Shenoi, S.S.C., Ethe, C., Madec, G., 2004. Impact of temperature inversions on SST evolution in the southeastern Arabian Sea during the pre-summer monsoon season. Geophys. Res. Lett. 31, L01305. http://dx.doi.org/10.1029/2003GL018906.

Durand, F., Shankar, D., de Boyer Montégut, C., Shenoi, S.S.C., Blanke, B., Madec, G., 2007. Modeling the barrier-layer formation in the South-Eastern Arabian Sea. J. Clim. 20, 2109–2120. http://dx.doi.org/10.1175/JCLI4112.1.

Durand, F., Shankar, D., Birol, F., Shenoi, S.S.C., 2008. Estimating boundary currents from satellite altimetry: a case study for the east coast of India. J. Oceanogr. 64, 831–845. http://dx.doi.org/10.1007/s10872-008-0069-2.

Durand, F., Shankar, D., Birol, F., Shenoi, S.S.C., 2009. Spatio-temporal structure of the East India Coastal Current from satellite altimetry. J. Geophys. Res. 114, C02013. http://dx.doi.org/10.1029/2008JC004807.

Durand, F., Papa, F., Rahman, A., Bala, S.K., 2011. Impact of Ganges–Brahmaputra interannual discharge variations on Bay of Bengal salinity and temperature during the 1992–99 period. J. Earth Syst. Sci. 120 (5), 859–872.

Gopalakrishna, V.V., Johnson, Z., Salgaonkar, G., Nisha, K., Rajan, C.K., Rao, R.R., 2005. Observed variability of sea surface salinity and thermal inversions in the Lakshadweep Sea during contrast monsoons. Geophys. Res. Lett. 32, L18605. http://dx.doi.org/10.1029/2005GL023280.

Han, W., McCreary, J.P., 2001. Modeling salinity distributions in the Indian Ocean. J. Geophys. Res. 106, 859–877.

Han, W., Webster, P.J., 2002. Forcing mechanisms of sea level interannual variability in the Bay of Bengal. J. Phys. Oceanogr. 32, 216–239.

Hoyos, C.D., Webster, P.J., 2007. The role of intraseasonal variability in the nature of Asian monsoon precipitation. J. Clim. 20, 4402–4424. http://dx.doi.org/10.1175/JCLI4252.1.

Huffman, G.J., Adler, R.F., Morrissey, M.M., Curtis, S., Joyce, R., McGavock, B., Susskind, J., 2001. Global precipitation at one-degree daily resolution from multi-satellite observations. J. Hydrometeor. 2, 36–50.

Jensen, T.G., 2001. Arabian Sea and Bay of Bengal exchange of salt and tracers in an ocean model. Geophys. Res. Lett. 28, 3967–3970.

Jensen, T.G., 2003. Cross-equatorial pathways of salt and tracers from the northern Indian Ocean: modelling results. Deep Sea Res. II 50, 2111–2127.

Jian, J., Webster, P.J., Hoyos, C.D., 2009. Large-scale controls on Ganges and Brahmaputra river discharge on intraseasonal and seasonal time-scales. Q. J. R. Meteorol. Soc. 135, 353–370. http://dx.doi.org/10.1002/qj.384.

Kantha, L., Rojsiraphisal, T., Lopez, J., 2008. The North Indian Ocean circulation and its variability as seen in a numerical hindcast of the years 1993–2004. Prog. Oceanogr., 0079-6611 76 (1), 111–147. http://dx.doi.org/10.1016/j.pocean.2007.05.006.

Koch Larrouy, A., Madec, G., Bouruet Aubertot, P., Gerkema, T., Bessières, L., Molcard, R., 2006. On the transformation of Pacific water into Indonesian throughflow water by internal tidal mixing. Geophys. Res. Lett. 34, L04604.

Large, W. G., Yeager, S., 2004. Diurnal to decadal global forcing for ocean and sea-ice models: the data sets and flux climatologies. NCAR Technical Note, NCAR/TN-460+STR, CGD Division of the National Center for Atmospheric Research.

Le Sommer, J., Penduff, T., Theetten, S., Madec, G., Barnier, B., 2009. How momentum advection schemes influence current-topography interactions at eddy-permitting resolution. Ocean Modell. 29 (1), 1–14.

Lévy, M., Estubier, A., Madec, G., 2001. Choice of an advection scheme for biogeochemical models. Geophys. Res. Lett. 28, 3725–3728.

Lévy, M., Iovino, D., Resplandy, L., Klein, P., Tréguier, A.-M., Madec, G., Masson, S., Takahashi, S., 2012. Large-scale impacts of submesoscale dynamics on phytoplankton: local and remote effects. Ocean Modell. 43–44, 77–93. http://dx.doi.org/10.1016/j.ocemod.2011.12.003.

Lukas, R., Lindstrom, E., 1991. The mixed layer of the western equatorial Pacific Ocean. J. Geophys. Res. 96, 3343–3358.

Madec, G, 2008. NEMO reference manual, ocean dynamics component. Note du pôle de modélisation, IPSL, France No. 27 ISSN No: 1288-1619.

Marchesiello, P., McWilliams, J.C., Shchepetkin, A.F., 2001. Open boundary conditions for long-term integration of regional ocean models. Ocean Modell. 3, 1–20.

Marchesiello, P., Capet, X., Menkes, C.E., Kennan, S.C., 2011. Submesocale dynamics in tropical instability waves. Ocean Modell. 39, 31–46.

Mariano, A.J., Ryan, E.H., Perkins, B.D., Smithers, S., 1995. The mariano global surface velocity analysis 1.0. Rep. CG-D-34-95, 55pp, US Coast Guard, Washington, DC.

McCreary, J.P., Kundu, P.K., Molinari, R.L., 1993. A numerical investigation of the dynamics, thermodynamics and mixed-layer processes in the Indian Ocean. Prog. Oceanogr. 31, 181–244. http://dx.doi.org/10.1016/0079-6611(93)90002-U.

McCreary, J.P., Han, W., Shankar, D., Shetye, S.R., 1996. Dynamics of the East India Coastal current 2. Numerical solutions. J. Geophys. Res. 101, 13,993–14,010. http://dx.doi.org/10.1029/96JC00560.

Mignot, J., de Boyer Montégut, C., Lazar, A., Cravatte, S., 2007. Control of salinity on the mixed layer depth in the world ocean: 2. Tropical areas. J. Geophys. Res. 112, C10010. http://dx.doi.org/10.1029/2006JC003954.

Murty, V.S.N., Sarma, Y.V.B., Rao, D.P., 1996. Variability of the oceanic boundary layer characteristics in the northern Bay of Bengal during MONTBLEX-90. Proc. Indian Acad. Sci. 105, 41–61.

Neetu, S., Lengaigne, M., Vincent, E.M., Vialard, J., Madec, G., Samson, G., RameshKumar, M.R., Durand, F., 2012. Influence of upper-ocean stratification on tropical cyclone-induced surface cooling in the Bay of Bengal. J. Geophys. Res. http://dx.doi.org/10.1029/2012JC008433.

Papa, F., Durand, F., Rahman, A., Bala, S.K., Rossow, W.B., 2010. Satellite altimeter-derived monthly discharge of the Ganga–Brahmaputra River and its seasonal to interannual variations from 1993 to 2008. J. Geophys. Res. 115, C12013. http://dx.doi.org/10.1029/2009JC006075.

Papa, F., Bala, S.K., Pandey, R.K., Durand, F., Gopalakrishna, V.V., Rahman, A., Rossow, W.B., 2012. Ganga–Brahmaputra river discharge from Jason-2 radar altimetry: an update to the long-term satellite-derived estimates of continental freshwater forcing flux into the Bay of Bengal. J. Geophys. Res. 117, C11021. http://dx.doi.org/10.1029/2012JC008158.

Parampil, S.R., Gera, A., Ravichandran, M., Sengupta, D., 2010. Intraseasonal response of mixed layer temperature and salinity in the Bay of Bengal to heat and freshwater flux. J. Geophys. Res. 115, C05002. http://dx.doi.org/10.1029/2009JC005790.

Penduff, T., Le Sommer, J., Barnier, B., Tréguier, A.M., Molines, J.M., Madec, G., 2007. Influence of numerical schemes on current- topography interactions in a 1/4° global ocean simulations. Ocean Sci. 3, 5509–5524.

Rao, R.R., Sivakumar, R., 2003. Seasonal variability of sea surface salinity and salt budget of the mixed layer of the north Indian Ocean. J. Geophys. Res. 108 (C1), 3009. http://dx.doi.org/10.1029/2001JC000907.

Roullet, G., Madec, G., 2000. Salt conservation, free surface, and varying levels: a new formulation for ocean general circulation models. J. Geophys. Res. 105, 23,927–23,942.

Sengupta, D., Bharath Raj, G.N., Shenoi, S.S.C., 2006. Surface freshwater from Bay of Bengal runoff and Indonesian throughflow in the tropical Indian Ocean. Geophys. Res. Lett. 33, L22609. http://dx.doi.org/10.1029/2006GL027573.

Sengupta, D., Bharath Raj, G., Anitha, D.S., 2008. Cyclone-induced mixing does not cool SST in the post-monsoon north Bay of Bengal. Atmos. Sci. Lett. 9, 1–6.

Shankar, D., 2000. Seasonal cycle of sea level and currents along the coast of India. Curr. Sci. 78 (3), 279–288.

Shankar, D., McCreary, J.P., Han, W., Shetye, S.R., 1996. Dynamics of the East India Coastal Current 1. Analytic solutions forced by interior Ekman pumping and local alongshore winds. J. Geophys. Res. 101, 13,975–13,991. http://dx.doi.org/10.1029/96JC00559.

Shankar, D., Vinayachandran, P.N., Unnikrishnan, A.S., 2002. The monsoon currents in the north Indian Ocean. Progr. Oceanogr. 52, 63–120.

Sharma, R., Agarwal, N., Momin, I.M., Basu, S., Agarwal, V.K., 2010. Simulated sea surface salinity variability in the tropical Indian Ocean. J. Clim. 23, 6542–6554. http://dx.doi.org/10.1175/2010JCLI3721.1.

Shenoi, S.S.C., Saji, P.K., Almeida, A.M., 1999. Near-surface circulation and kinetic energy in the tropical Indian Ocean derived from Lagrangian drifters. J. Mar. Res. 57, 885–907.

Shenoi, S.S.C., Shankar, D., Shetye, S.R., 2002. Differences in heat budgets of the near-surface Arabian Sea and Bay of Bengal: implications for the summer monsoon. J. Geophys. Res. 107, 3052. http://dx.doi.org/10.1029/2000JC000679.

Shetye, S.R., 1993. The movement and implications of the Ganges–Bramhaputra runoff on entering the Bay of Bengal. Curr. Sci. 64 (1), 32–38.

Shetye, S.R., Shenoi, S.S.C., Gouveia, A.D., Michael, G., Sundar, S., Nampoothiri, G., 1991. Wind-driven coastal upwelling along the western boundary of the Bay of Bengal during the southwest monsoon. Cont. Shelf Res. 11, 1397–1408.

Shetye, S.R., Gouveia, A.D., Shankar, D., Shenoi, S.S.C., Vinayachandran, P.N., Sundar, D., Michael, G.S., Nampoothiri, G., 1996. Hydrography and circulation in the western Bay of Bengal during the northeast monsoon. J. Geophys. Res. 101, 14011–14025. http://dx.doi.org/10.1029/95JC03307.

Skamarock, W.C., 2004. Evaluating mesoscale NWP models using kinetic energy spectra. Mon. Weather Rev. 132, 3019–3032. http://dx.doi.org/10.1175/MWR2830.1.

Sudre, J., Maes, C., Garçon, V., 2013. On the global estimates of geostrophic and Ekman surface currents. Limnol. Oceanogr.: Fluids Environ. 3, 1–20. http://dx.doi.org/10.1215/21573689.

Thadathil, P., Gopalakrishna, V.V., Muraleedharan, P.M., Reddy, G.V., Araligidad, N., Shenoy, S., 2002. Surface layer temperature inversion in the Bay of Bengal. Deep Sea Res. Part I 49, 1801–1818.

Thadathil, P., Muraleedharan, P.M., Rao, R.R., Somayajulu, Y.K., Reddy, G.V., Revichandran, C., 2007. Observed seasonal variability of barrier layer in the Bay of Bengal. J. Geophys. Res. 112, C02009. http://dx.doi.org/10.1029/2006JC003651.

Vecchi, G.A., Harrison, D.E., 2002. Monsoon breaks and subseasonal sea surface temperature variability in the Bay of Bengal. J. Clim. 15, 1485–1493.

Vinayachandran, P.N., Kurian, J., 2007. Hydrographic observations and model simulation of the Bay of Bengal freshwater plume. Deep Sea Res. Part I 54, 471–486.

Vinayachandran, P.N., Murty, V.S.N., Ramesh Babu, V., 2002. Observations of barrier layer formation in the Bay of Bengal during summer monsoon. J. Geophys. Res. 107 (C12), 8018. http://dx.doi.org/10.1029/2001JC000831.

Vinayachandran, P.N., Neema, C.P., Mathew, S., Remya, R., 2012. Mechanisms of summer intraseasonal sea surface temperature oscillations in the Bay of Bengal. J. Geophys. Res. 117, C01005. http://dx.doi.org/10.1029/2011JC007433.

Webster, P.J. et al., 2002. The jasmine pilot study. Bull. Am. Metrol. Soc., 1603–1630.

Wentz, F.J., Gentemann, C., Smith, D., Chelton, D., 2000. Satellite measurements of sea-surface temperature through clouds. Science 288, 847–850.

Wu, L., Wang, F., Yuan, D., Cui, M., 2007. Evolution of freshwater plumes and salinity fronts in the northern Bay of Bengal. J. Geophys. Res. 112, C08017. http://dx.doi.org/10.1029/2005JC003308.

Xie, P., Arkin, P., Janowiak, J., 2007. CMAP: The CPC merged analysis of precipitation, in Measuring Precipitation from Space. In: Levizzani, V, Bauer, P., Turk, F.J. (Eds.), Adv. Global Change Res, vol. 28. Springer, Dordrecht, Netherlands, pp. 319–328. http://dx.doi.org/10.1007/978-1-4020-5835-6_25.

Yaremchuk, M., 2006. Sea surface salinity constrains rainfall estimates over tropical oceans. Geophys. Res. Lett. 33, L15605. http://dx.doi.org/10.1029/2006GL026582.

Yaremchuk, M., Yu, Z., McCreary, J., 2005. River discharge into the Bay of Bengal in an inverse ocean model. Geophys. Res. Lett. 32, L16605. http://dx.doi.org/10.1029/2005GL023750.

Yu, Z., McCreary Jr., J.P., 2004. Assessing precipitation products in the Indian Ocean using an ocean model. J. Geophys. Res. 109, C05013. http://dx.doi.org/10.1029/2003JC002106.